

Article

# Mesozoic High- and Low-SiO<sub>2</sub> Adakites and A-Type Granites in the Lower Yangtze River Belt, Eastern China: Implications for Petrogenesis and Metallogeny

Lei Liu <sup>1</sup>, Geng Chu <sup>1</sup>, Yanguang Li <sup>2,3,\*</sup>, Xiaoyong Yang <sup>1,\*</sup>, M. Santosh <sup>4,5</sup> and Qing Hu <sup>1</sup>

<sup>1</sup> CAS Key Laboratory of Crust-Mantle Materials and Environments, School of Earth and Space Sciences, University of Science and Technology of China, 96 Jinzhai Road, Hefei 230026, China; liu01@ustc.edu.cn (L.L.); gengchu@live.cn (G.C.); qing123@mail.ustc.edu.cn (Q.H.)

<sup>2</sup> MLR Key Laboratory for the Study of Focused Magmatism and Giant Ore Deposits, Xi'an Center of Geological Survey, CGS, Xi'an 710054, China

<sup>3</sup> Center for Orogenic Belt Geology, Xi'an Center of Geological Survey, CGS, Xi'an 710054, China

<sup>4</sup> School of Earth Science and Resource, China University of Geosciences, Beijing 100083, China; msantosh.gr@gmail.com

<sup>5</sup> Department of Earth Sciences, University of Adelaide, Adelaide SA 5005, Australia

\* Correspondence: liyanguangok@126.com (Y.L.); xyang555@163.com (X.Y.); Tel.: +86-551-6360-p6871 (X.Y.)

Received: 8 June 2018; Accepted: 26 July 2018; Published: 30 July 2018



**Abstract:** The Lower Yangtze River Belt (LYRB) is one of the important magmatic and metallogenic belts in China and hosts abundant Mesozoic calc-alkaline magmatic rocks and economic mineral deposits. Anqing orefield in the southwestern of the LYRB received less attention during the last two decades. Here, we present an integrated study of whole-rock major and trace elements, zircon U-Pb dating and Lu-Hf isotopes on late Mesozoic adakites and A-type granites from the Anqing orefield. The adakites emplaced during 138–136 Ma and can be further subdivided into two types: high-SiO<sub>2</sub> adakites (HSA) with SiO<sub>2</sub> >60 wt % from the Zongpu intrusion, and low-SiO<sub>2</sub> adakites (LSA) <60 wt % from the Yueshan intrusion. The rocks display mid- to high-K calc-alkaline features and have consistent arc-like trace element characteristics with enrichment in LREE and LILE, and depletion in HREE and HFSE. The distinct zircon  $\varepsilon_{\text{Hf}}(t)$  values for the LSA (from −27 to −20) and HSA (from −15 to −5) preclude a magma mixing model, yet suggest a subduction-related setting with partial melting of the subducted slab and overlying metasomatic mantle wedge. The A-type granites dated at 124 Ma from the Dalongshan intrusion characterized by LILE and LREE enrichment and slightly negative Eu anomalies, with lower MgO, CaO but higher K<sub>2</sub>O and Na<sub>2</sub>O contents. Their zircon  $\varepsilon_{\text{Hf}}(t)$  values and geochemical features suggest that the parent magma was produced by the partial melting of Neoproterozoic crustal components, followed by variable degrees of fractional crystallization under a back-arc extensional setting, together with minor juvenile crust input. The adakites and A-type granites investigated in this study record a tectonic transition from compressive to extensional setting during 138–124 Ma. The transitional magmatic pulses are associated with distinct metallogenic signature with the adakites hosting copper deposits and the A-type granites linked to uranium mineralization.

**Keywords:** Adakite; A-type granite; Tectonic transition; Subduction; Lower Yangtze River Belt (LYRB)

## 1. Introduction

The Lower Yangtze River Belt (LYRB) in China has been the focus of several geological, geochemical and geochronological studies in relation to the voluminous magmatism and associated metallogeny [1–14]. The LYRB hosts abundant Mesozoic calc-alkaline magmatic rocks with spatially

and genetically ore deposits [10]. The petrogenesis of these magmatic suites provide insights on the metallogeny. Previous studies have proposed diverse models on the genesis of these rocks such as: (1) mixing of melts from enriched mantle and lower continental crust (LCC) [11,13]; (2) partial melting of subducted slab or ridge subduction followed by crustal assimilation [6,7,9,12]. The former model envisages an extensional setting for the calc-alkaline magmatic rocks, whereas the latter proposes a compressional setting.

In order to address this controversy, we investigated adakites and A-type granites from this belt. Defant and Drummond [15] following the work of Kay [16] first defined adakites from magnesian andesites in Adak Island in Aleutian and refer to magmas derived from the melting of young subducted lithosphere, with high Sr/Y and La/Yb ratios. Martin et al. [17] discriminated adakites into: high-SiO<sub>2</sub> adakites (HSA; SiO<sub>2</sub> >60 wt %) and low-SiO<sub>2</sub> adakites (LSA; SiO<sub>2</sub> <60 wt %). The HSA is considered to be generated by partial melting of a hydrous subducted slab, whereas LSA forms from partial melts of peridotitic mantle wedge metasomatised by HSA or subduction-dehydration fluids. In addition, Zhang et al. [18] proposed a new term of continental adakite based on the Yanshanian magmatic rocks in East China, and termed these as C-type adakite in contrast to the oceanic slab related adakite (O-type adakite). The C-type adakite is formed by partial melting of thickened lower crust or by fractional crystallization and is enriched in potassium [18,19] in contrast to O-type adakite which is characterized by sodium enrichment. Therefore, characterizing adakitic rocks is fundamental to the understanding of the tectonic settings and petrogenetic history of these intermediate and felsic magmatic suites.

A-type granites are generally considered to form in extensional tectonic settings [20,21]. Late Mesozoic A-type granites are widely distributed in LYRB, with ages in the range of 129–122 Ma, and their appearance is considered to mark a dominant extensional environment in this region [22,23]. Although A-type granites are characterized by anhydrous, alkaline and anorogenic features, their origin is also debated, particularly those in eastern China [24]. The popular models of their genesis include: (1) low-pressure melting of calc-alkaline rocks at upper crustal levels [25]; and (2) hybridization between anatectic granitic and mantle-derived magmas [26].

The Anqing orefield in the Anqing–Guichi area, is among the seven major polymetallic domains in the LYRB [1,2]. The Cu-Fe-Au ore deposits in this region are related to adakite intrusions [27]. Wang et al. [28] proposed that the adakite intrusions were derived from dehydration melting of delaminated mafic lower crust in an extensional tectonic regime within continental setting. On the other hand, the major hydrothermal uranium ore deposit at the Dalongshan is associated with A-type granite [29]. Thus, the late Mesozoic adakite and A-type granite intrusions in this area provide a window to explore magma evolution, tectonic setting and the relation with metallogeny. With this objective, we present an integrated study of whole-rock major and trace elements, zircon U-Pb dating and Lu-Hf isotopes on the adakites and A-type granites.

## 2. Geological Setting and Samples

The LYRB is located in the northern margin of the Yangtze Block along the central and lower drainage area of the Yangtze River, extending 400 km from southwestern Hubei to northeastern Jiangsu (Figure 1a [10]). Three major fault zones have been delimited in the LYRB area, including Xiangfan–Guangji Fault (XGF) in the southwest, Tancheng–Lujiang Fault (TLF) in the northwest and Yangxin–Changzhou Fault (YCF) in the south and southeast (Figure 1a). The metamorphic basement rocks in the Yangtze Block are composed of amphibolites and granulite-facies biotite-hornblende gneisses, TTG (tonalite-trondhjemite-granodiorite) and supracrustal rocks [1]. The Paleoproterozoic (>3.3 Ga) Kongling Group is regarded as the oldest basement, which is overlain by 2000 m thick Paleoproterozoic to Neoproterozoic (1850–990 Ma) volcano-sedimentary succession [2]. Widespread Neoproterozoic magmatic events produced voluminous bimodal volcanic rocks during 825–740 Ma and involved partial reworking of the older basement. The younger rock suites are represented by the Neoproterozoic Shangxi Group and Jingtian Formation low grade metamorphic rocks and volcanic rocks in south Anhui. The LYRB is characterized by extensive late Mesozoic magmatism

and mineralization, and is the most important source for metallic ores in eastern China [1,10]. The large-scale mineralization in this region is strongly associated with extensive late Mesozoic magmatism, as evidenced by the fact that the Cu-Au deposits are closely associated with late Jurassic to early Cretaceous intermediate to felsic high-K calc-alkaline rocks both spatially and temporally. Geochemical evidence indicate these rocks belong to adakites [12,30,31]. Two parallel A-type granites belt have been identified in the LYRB (Figure 1a), both in the uplifted zones and fault zones [32], which was formed at ca. 125 Ma, represented the final stage of ore-related magmatism.

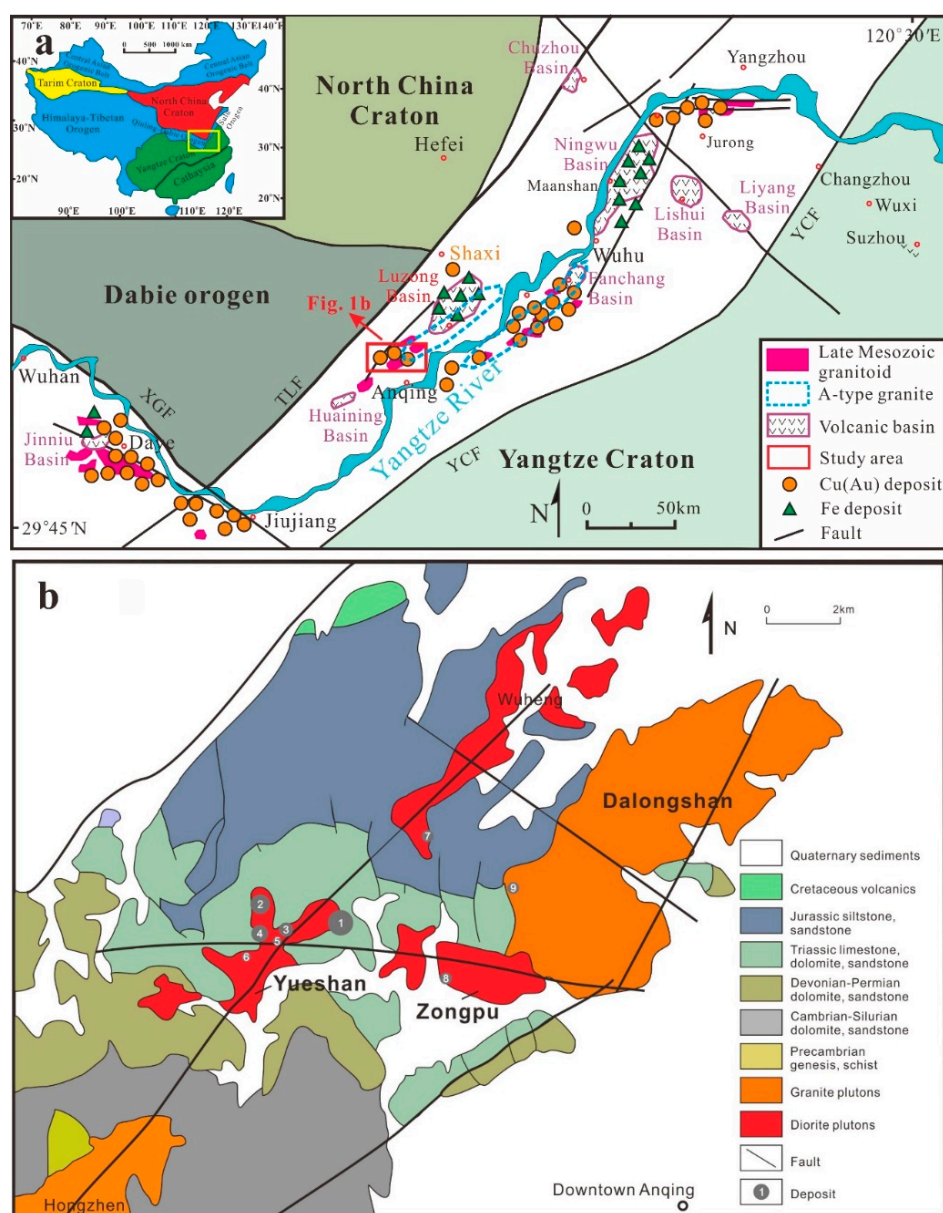


**Figure 1.** (a) Simplified geological map of magmatic rocks and ore deposits in the LYRB (the insert shows the general tectonic divisions of China (modified after [11,33,34])); (b) geological map of the Anqing district, Anhui Province, China (modified after [27]). YCF: Yangxin–Changzhou Fault, XGF: Xiangfan–Guangji Fault, TLF: Tancheng–Lujiang Fault. Ore deposit information: 1—Anqing copper deposit; 2—Tongliujing deposit; 3—Tiepuling deposit; 4—Liujiawa deposit; 5—Longmenshan copper deposit; 6—Dapai iron deposit; 7—Yanjialaowu deposit; 8—Caiguashan deposit; 9—Dalongshan deposit. The Yueshan, Zongpu, Dalongshan, Wuheng and Hongzhen intrusions are shown (from [27]).

The Anqing orefield is located in the southwestern margin of LYRB. Tectonically, the region falls within the northern margin of the Yangtze Block, and was affected by the Yangtze deep fault zone (Figure 1b). The stratigraphic sequences of the Anqing orefield contain three major units: the Precambrian Dongling Formation, which represents the regional basement with an age of  $1895 \pm 38$  Ma [35]; Cambrian to Triassic sedimentary rocks, consisting of shallow-marine carbonate rocks, sandstone and shale; and Jurassic to Cretaceous sedimentary rocks, composed of continental clastic and volcanic rocks [36]. In this area, polymetallic Cu-Fe-Au-Mo-U-(Pb-Zn) deposits and uranium mineralization occur or adjacent to the Yanshanian intrusions which are emplaced within Permian, Triassic, and Jurassic sequences [37]. The intrusions are exposed as stocks, dikes and sills with different outcrop size ranging from 90 km<sup>2</sup> to less than 1 km<sup>2</sup> (Figure 1b [27]). They are dominantly composed of diorite, quartz monzodiorite, granodiorite and granite [1,27,36].

Many of the plutons intruded into the dolomite and brecciated limestone of the Triassic Yueshan and Lanlinghu Formations, and host Cu-Au skarn- and vein-type deposits (Figure 2a,d). Among these, the Yueshan diorite is the most important intrusion and hosts Cu-Fe-Au mineralization. The pluton is composed of diorite, quartz diorite and monzodiorite (Figure 3a,b). The quartz diorite shows medium- to fine-grained or inequigranular texture, and is composed of plagioclase (50%–70%), amphibole (10%–20%), K-feldspar (5%–15%), quartz (5%–15%), and minor biotite, pyroxene and accessory minerals including titanite, apatite and pyrite (Figure 3a,b).

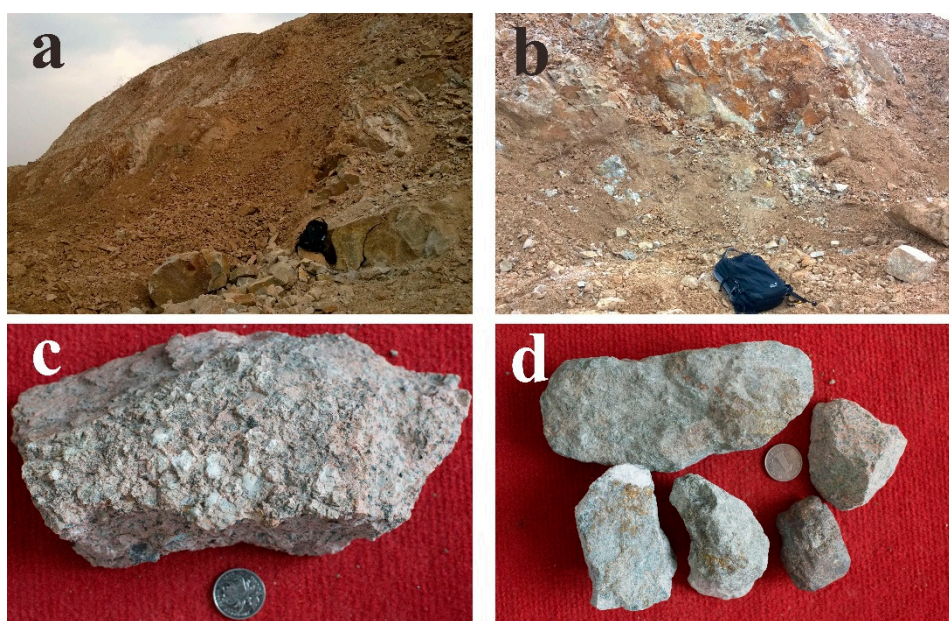


**Figure 2.** Field photos of the Yueshan (a) and the Zongpu intrusions (b); hand specimens of the Dalongshan quartz granite porphyry (c) and the Yueshan quartz diorite and ores (d).

The Zongpu diorite pluton consists of quartz diorite and granodiorite with fine- to medium-grained granular and porphyritic textures (Figures 2b and 3c,d). The mineral assemblage is similar to that in the Yueshan intrusion, except for the higher biotite and lower amphibole contents in the Zongpu diorite. The Dalongshan A-type granite in the western part of the Zongpu intrusion is associated with hydrothermal uranium deposits. The pluton is composed of quartz–syenite and alkali–feldspar–granite, with fine to medium granular texture, and an assemblage comprising perthite (25%–35%), quartz (30%–35%), orthoclase (10%–15%), plagioclase (10%–15%), amphibole (3%–8%), biotite (2%–5%), and minor accessory minerals (pyrite, magnetite and apatite) [33] (Figures 2c and 3e,f).

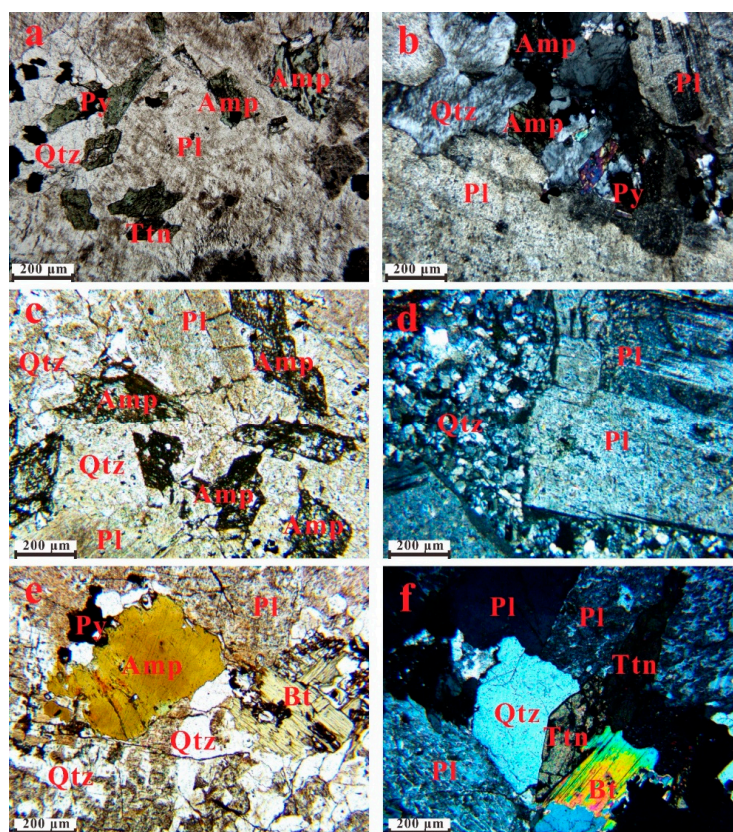


**Figure 3.** Photomicrographs of the Yueshan, Zongpu and Dalongshan intrusive rocks in the Anqing orefield. The Yueshan quartz diorite shows Amp + Pl + Qtz and accessory titanite and pyrite; plane polarized light (a) and cross polarized light (b). The Zongpu quartz diorite mainly composed of plagioclase, perthite, quartz and amphibole, shown in plane polarized light (c) and cross polarized light (d). The Dalongshan quartz granite porphyry showing plagioclase, quartz, biotite and amphibole in plane polarized light (e) and cross polarized light (f). Amp: amphibole, Bt: biotite, Pl: plagioclase, Py: pyrite, Qtz: quartz, Ttn: titanite.

### 3. Analytical Methods

#### 3.1. Whole-Rock Major and Trace Element Analysis

Fresh samples were powdered in an agate mill to <200 mesh size at the ALS Geochemistry Laboratory in Guangzhou. Major oxides were determined by wavelength-dispersive X-ray fluorescence spectrometry (XRF) on fused glass beads using an AXIOS Minerals spectrometer at ALS. Loss on ignition (LOI) was determined after igniting the sample powders at 1000 °C for 1 h. The analytical uncertainties were generally within 0.1%–1% (RSD). Trace elements, including rare earth elements (REE), were determined by inductively coupled plasma mass spectrometry (ICPMS) of solutions on an Elan DRC-II instrument (Element, Finnigan MAT), after 2 days closed beaker digestion using a mixture of HF and HNO<sub>3</sub> acids in Teflon screw-cap bombs. The uncertainties of the ICPMS analyses are estimated to be better than 5% for most elements.

#### 3.2. LA-ICPMS Zircon U-Pb Dating

Zircon grains were separated from samples using standard density and magnetic separation techniques. Representative zircon grains were hand-picked under a binocular microscope, mounted on adhesive, enclosed in epoxy resin, polished, and photographed in reflected light. The internal structure of the grains was examined using the cathodoluminescence (CL) image at the Analytical Center of

University of Science and Technology of China in Hefei. Zircon U-Pb analysis was conducted by Laser Ablation- Inductively Coupled Plasma Mass Spectrometry (LA-ICPMS) at the CAS Key Laboratory of Crust-Mantle Materials and Environments, University of Science and Technology of China in Hefei. The GeoLas 200M laser-ablation system is equipped with a 193 nm ArF-excimer laser was used in connection with ELAN6100 DRC ICPMS in Hefei. Helium gas was used as the carrier gas to enhance the transport efficiency of the ablated material. All measurements were performed using zircon 91500 as the external standard with a recommended  $^{206}\text{Pb}/^{238}\text{U}$  age of  $1065.4 \pm 0.6$  Ma [38]. Common Pb correction was carried out by using the EXCEL program of ComPbCorr#3\_181 [39]. Ages were calculated using the ISOPLOT program [40].

### 3.3. Zircon Lu-Hf Isotope Analysis

In-situ analyses of Lu-Hf isotopes were conducted by laser ablation of the same zircon grains on the spots previously analyzed by LA-MC-ICPMS. Analyses were carried out using a New Wave—193 nm ArF-excimer laser-ablation system linked to a Neptune multiple-collector inductively coupled plasma mass spectrometer (LA-MC-ICPMS), housed at the laboratory of the Tianjin Institute of Geology and Mineral Resource, Chinese Academy of Geological Sciences. Instrumental parameters and data acquisition followed that described by Wu et al. [41]. The analyses were conducted with a beam diameter of 50  $\mu\text{m}$ , 8 Hz repetition rate with a laser power of 15 J/cm<sup>2</sup>. External calibration was made by measuring zircon standard GJ-1 with the unknowns during the analyses to evaluate the reliability of the analytical data, which yielded a weighted mean  $^{176}\text{Hf}/^{177}\text{Hf}$  ratio of  $0.282001 \pm 37$  ( $2\sigma$ ). This value is in good agreement with the recommended value of  $0.282008 \pm 7$  ( $2\sigma$ ) [42]. The mean  $\beta\text{Yb}$  value was applied for the isobaric interference correction of  $^{176}\text{Yb}$  on  $^{176}\text{Hf}$  in the same spot. The ratio of  $^{176}\text{Yb}/^{172}\text{Yb}$  (0.5887) was also applied for the Yb correction. A decay constant for  $^{176}\text{Lu}$  of  $1.865 \times 10^{-11}$  year<sup>-1</sup> [43], the present-day chondritic ratios  $^{176}\text{Hf}/^{177}\text{Hf} = 0.282772$  and  $^{176}\text{Lu}/^{177}\text{Hf} = 0.0332$  [42] were adopted to calculate  $\epsilon_{\text{Hf}}(t)$  values. Single-stage Hf model ages ( $T_{\text{DM1}}$ ) were calculated relative to the depleted mantle present-day value of  $^{176}\text{Hf}/^{177}\text{Hf} = 0.28325$  and  $^{176}\text{Lu}/^{177}\text{Hf} = 0.0384$  [44]. The two-stage Hf model ages ( $T_{\text{DM2}}$ ) were calculated assuming that the parental magma was produced from average continental crust ( $^{176}\text{Lu}/^{177}\text{Hf} = 0.015$ ) that originally was derived from the depleted mantle [45].

### 3.4. Zircon Trace Element Analysis

Zircon trace element analyses were performed by LA-ICPMS at the CAS Key Laboratory of Crust-Mantle Materials and Environments, University of Science and Technology of China in Hefei. The laser ablation spots are close to the LA-ICPMS analysis spots on the same zircon grain. Analyses of zircon trace elements were conducted with a beam diameter of 32  $\mu\text{m}$ , repetition rate of 6 Hz and laser energy of 60 mJ. The detailed parameters of the instrument can be found in Liu et al. [46], and the analytical procedures were previously reported by Yuan et al. [47]. Quantitative results were obtained through calibration of relative element sensitivities using the NIST-610 as the external standard, and the zircon  $\text{SiO}_2$  as an internal standard for normalization of each analysis. The precision of simultaneous NIST-610 analyses is better than 5% for REE, Y, Sr, Nb, Hf, Ta, Th and U at the ppm level, and better than 10% for Mn, P, Ti and Pb. The detection limit for the different REE varies from 0.02 to 0.09 ppm.

## 4. Results

### 4.1. Major and Trace Elements

A total of fifteen samples (including seven diorites in the Yueshan, six diorites in the Zongpu and two granites in the Dalongshan) from the Anqing orefield were selected for whole-rock major and trace elements analyses and the results are listed in Table 1. In addition, published data from this area are also compiled [48–52], they are listed in Supplementary data Table S1.

The diorites show  $\text{SiO}_2$  contents ranging from 56.33 to 68.43 wt % with an average of 59.89 wt %, whereas their total alkali contents ( $\text{K}_2\text{O} + \text{Na}_2\text{O}$ ) vary from 6.68 wt % to 9.94 wt %, with a mean of 8.02 wt % (statistical data from Table 1 and Table S1, same as follow). The rocks show high  $\text{Na}_2\text{O}$  contents of 4.09 wt %–6.22 wt % with mean of 5.00 wt %. Following the definition by Martin et al. [17], the HSA dominantly occur in the Zongpu ( $\text{SiO}_2 > 60$  wt %), whereas the LSA are mainly distributed in the Yueshan ( $\text{SiO}_2 < 60$  wt %). Both rock types are enriched in  $\text{Al}_2\text{O}_3$  from 14.45 to 18.12 wt % with an average of 16.29 wt %. Furthermore, the LSA have higher MgO contents relative to HSA with Mg# (molar ration of  $\text{Mg}^{2+}/[\text{Mg}^{2+} + \text{Fe}^{2+}]$ ) of 47 to 52. In contrast, the granites from the Dalongshan have higher  $\text{SiO}_2$  and  $\text{K}_2\text{O}$  contents, but lower CaO and MgO relative to diorites. Their Mg# shows values down to 21, far lower than the adakites nearby.

We used TAS (Total Alkali vs.  $\text{SiO}_2$ ) diagram (Figure 4a) and  $\text{K}_2\text{O}$ - $\text{SiO}_2$  diagram (Figure 4b) to classify the intrusions in the Anqing orefield. In the TAS diagram, both the Yueshan and Zongpu diorites are mainly located within monzonite field with several high- $\text{SiO}_2$  samples falling in the quartz-monzonite zone, whereas the Dalongshan granites are located in the syenite and granite fields. In  $\text{K}_2\text{O}$ - $\text{SiO}_2$  diagram, the Yueshan diorites dominantly belong high-K calc-alkaline series, and the Zongpu diorites display calc-alkaline affinity, also refer to Figure S1. The Dalongshan granites have very high  $\text{K}_2\text{O}$  contents, and plot within shoshonitic series with marked variation in their  $\text{SiO}_2$  contents.

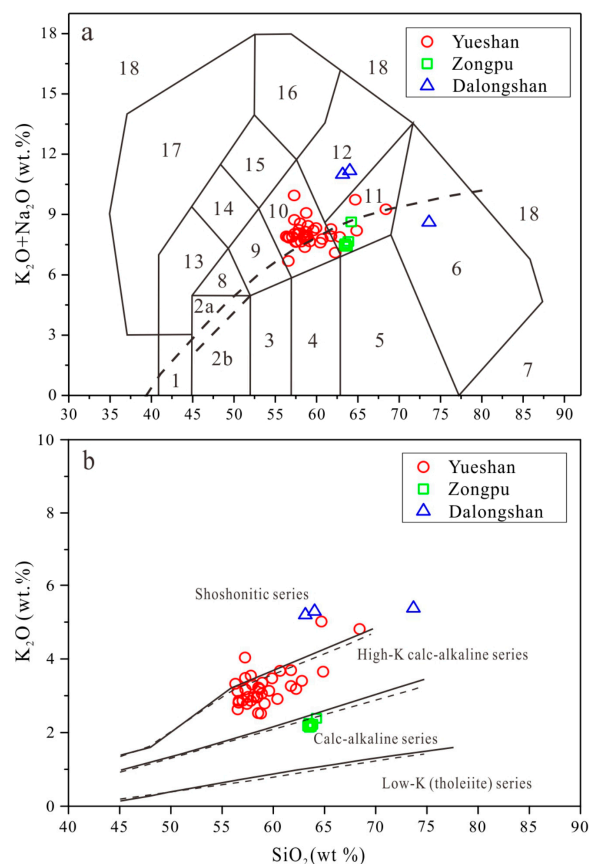


**Figure 4.** TAS (a) and  $\text{K}_2\text{O}$ - $\text{SiO}_2$  (b) classification diagrams for the Yueshan, Zongpu and Dalongshan magmatic rocks. Fields in the TAS diagram are after [53]. The fields for  $\text{K}_2\text{O}$ - $\text{SiO}_2$  diagram are after [54], and the dashed line is from [53]. 1—olivine gabbro; 2a—syenogabbro; 2b—gabbro; 3—gabbro– diorite; 4—diorite; 5—granodiorite; 6—granite; 8—alkali–gabbro; 9—alkali–gabbroidiorite; 10—syenodiorite; 11—quartz monzonite; 12—syenite; 13—feldspathoid gabbro; 14—feldspathoid monzonite diorite; 15—feldspathoid monzonitic syenite; 16—feldspathoid syenite; 17—foiidite pluton; 18—leucite rock.

**Table 1.** Major and trace element compositions of the Yueshan, Zongpu and Dalongshan intrusions in the Anqing orefield.

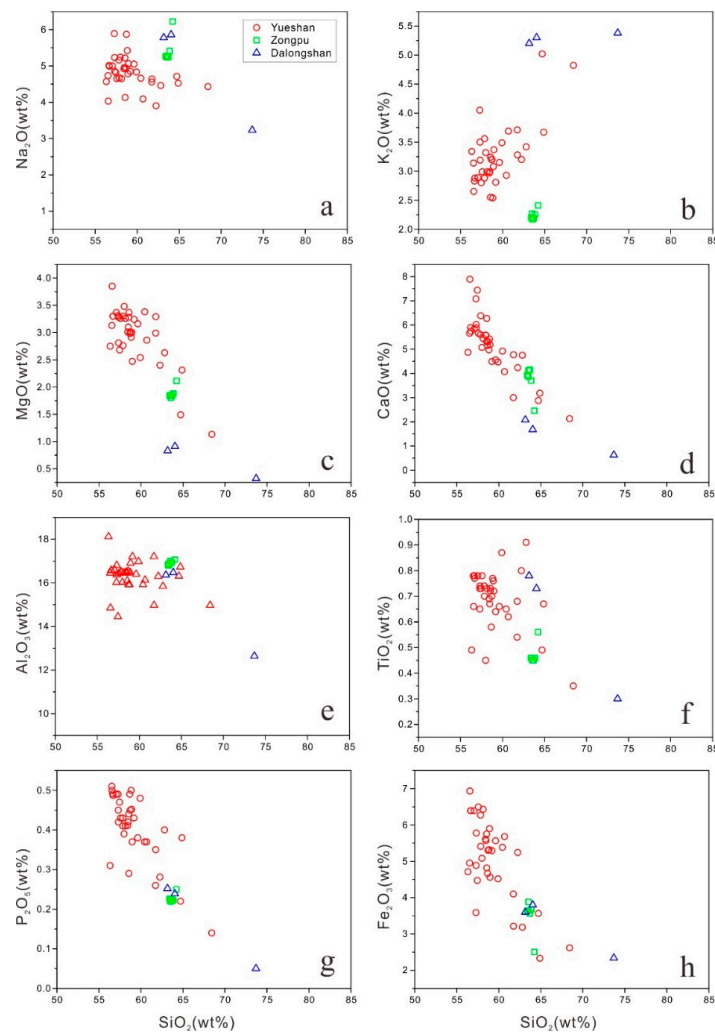
Samples	YS18	14YS01	14YS02	14YS03	14YS04	14YS05	14YS06	03ZPS02	14ZP01	14ZP02	14ZP03	14ZP04	14ZP05	14DLS01	14DLS02
Intrusion	Yueshan	Zongpu	Zongpu	Zongpu	Zongpu	Zongpu	Zongpu	Dalongshan	Dalongshan						
Major oxides (wt %)															
SiO <sub>2</sub>	62.26	57.06	58.43	58.91	58.49	56.68	56.66	64.23	63.71	63.54	63.50	63.41	63.86	64.04	63.16
Al <sub>2</sub> O <sub>3</sub>	16.30	16.59	16.50	16.48	16.45	16.56	16.58	17.06	17.00	16.88	16.80	16.83	16.92	16.47	16.36
Fe <sub>2</sub> O <sub>3</sub>	5.24	6.39	5.61	5.90	5.57	6.39	6.39	2.50	3.56	3.88	3.64	3.63	3.67	3.80	3.60
CaO	4.24	5.83	5.58	5.42	5.57	5.74	5.89	2.46	4.15	4.12	3.87	3.93	3.70	1.68	2.08
MgO	2.40	3.37	3.01	3.00	3.10	3.30	3.30	2.11	1.84	1.80	1.85	1.84	1.88	0.91	0.83
Na <sub>2</sub> O	3.90	5.00	4.92	4.78	4.96	4.99	5.01	6.22	5.24	5.24	5.27	5.26	5.41	5.86	5.78
K <sub>2</sub> O	3.20	2.89	2.97	3.08	2.99	2.88	2.83	2.41	2.19	2.17	2.27	2.20	2.25	5.30	5.20
TiO <sub>2</sub>	0.80	0.78	0.69	0.76	0.67	0.77	0.78	0.56	0.45	0.45	0.46	0.46	0.46	0.73	0.78
MnO	0.09	0.10	0.09	0.10	0.10	0.10	0.10	0.02	0.03	0.03	0.03	0.03	0.03	0.09	0.08
P <sub>2</sub> O <sub>5</sub>	0.281	0.490	0.411	0.452	0.420	0.487	0.491	0.250	0.226	0.219	0.223	0.226	0.222	0.239	0.252
LOI	0.75	1.14	0.82	0.70	0.86	1.11	0.92	1.07	1.06	1.04	1.19	1.14	1.28	0.64	1.10
Total	99.46	99.99	99.38	99.90	99.51	99.36	99.31	98.89	99.77	99.69	99.41	99.26	99.99	99.87	99.34
K <sub>2</sub> O/Na <sub>2</sub> O	0.82	0.58	0.60	0.64	0.60	0.58	0.56	0.39	0.42	0.41	0.43	0.42	0.42	0.90	0.90
Mg#	47.57	51.09	51.52	50.18	52.44	50.57	50.57	62.57	50.59	47.89	50.17	50.10	50.37	32.18	31.35
Trace elements (ppm)															
Ba	1670	1270	1240	1150	1310	1310	1240	242	1430	1430	1430	1450	1310	720	730
Cr	30	31	34	28	31	29	32	40	25	63	48	50	47	41	29
Hf	6	0.9	1.0	1.0	1.1	1.0	1.0	3.8	0.8	0.8	0.8	0.9	0.8	2.1	2.2
Nb	9.3	7.4	7.1	9.0	7.4	7.6	7.8	7.2	6.3	6.4	6.3	6.5	6.4	34.6	38.1
Ni	13	16.7	16.7	12.5	16.6	16.2	16.3	16	14.6	15.9	14.7	14.9	14.4	3.1	1.9
Pb	18	16.0	17.9	16.6	14.0	16.2	15.3	11	11.3	11.8	13.7	10.3	13.6	19.6	17.3
Rb	77.5	41.1	40.1	53.4	48.0	42.6	41.0	10.6	27.6	28.1	31.0	30.4	30.5	175.0	179.5
Sr	773	1800	1690	1600	1880	1880	1840	632	1570	1570	1470	1550	1420	296	306
Ta	0.5	0.32	0.34	0.47	0.33	0.35	0.36	0.3	0.34	0.37	0.36	0.36	0.35	2.06	2.34
Th	8.48	12.2	7.8	13.3	9.4	8.3	9.3	5.35	4.4	4.4	4.6	4.8	4.5	20.8	20.2
Ti	4796	4420	3940	4170	4070	4590	4450	3357	2590	2680	2660	2770	2570	4250	4670
U	1.63	2.3	2.4	2.7	2.8	2.1	2.4	1.63	1.0	1.0	1.0	1.0	1.0	3.1	3.0
Y	16.9	12.0	8.9	13.0	10.8	12.3	13.0	10.1	8.7	8.7	8.9	9.2	9.1	34.8	38.5
Zr	245	16.2	20.0	15.6	22.9	17.0	17.9	153	14.7	15.4	15.0	15.7	15.4	50.2	49.4
La	54	44.3	36.7	48.4	42.1	47.5	51.7	28.9	25.5	25.9	26.1	27.0	26.0	89.1	95.8
Ce	96.4	94.1	78.5	100.5	92.8	101.0	107.0	54.4	53.4	53.7	55.5	56.3	55.0	167.5	188.0
Pr	10.85	10.30	8.43	10.75	10.15	11.00	11.70	6.47	5.96	5.93	6.19	6.37	6.24	16.95	19.50
Nd	38	40.3	31.5	39.7	39.0	42.3	45.9	24.3	22.7	22.7	23.4	24.5	23.5	58.3	66.0
Sm	6.14	6.59	5.23	6.67	6.42	7.07	7.54	4.27	3.90	3.91	3.94	4.10	3.94	9.40	11.10
Eu	1.81	1.76	1.40	1.71	1.70	1.93	2.00	1.26	1.12	1.08	1.07	1.15	1.08	2.02	2.18
Gd	6.25	4.14	3.30	4.21	3.95	4.50	4.65	4.03	2.67	2.64	2.63	2.80	2.61	6.73	7.77
Tb	0.77	0.50	0.40	0.54	0.49	0.56	0.58	0.49	0.35	0.35	0.35	0.37	0.35	1.06	1.20

Table 1. Cont.

Samples	YS18	14YS01	14YS02	14YS03	14YS04	14YS05	14YS06	03ZPS02	14ZP01	14ZP02	14ZP03	14ZP04	14ZP05	14DLS01	14DLS02
Intrusion	Yueshan	Zongpu	Zongpu	Zongpu	Zongpu	Zongpu	Zongpu	Dalongshan	Dalongshan						
Dy	3.64	2.51	1.96	2.68	2.39	2.76	2.83	2.21	1.84	1.82	1.83	1.90	1.87	6.20	7.07
Ho	0.69	0.45	0.35	0.49	0.41	0.49	0.50	0.4	0.34	0.33	0.34	0.35	0.35	1.24	1.43
Er	1.97	1.17	0.89	1.31	1.11	1.30	1.30	1.15	0.93	0.91	0.91	0.95	0.94	3.68	4.29
Tm	0.27	0.16	0.12	0.18	0.15	0.17	0.17	0.15	0.13	0.13	0.13	0.13	0.13	0.56	0.64
Yb	1.71	1.00	0.82	1.20	0.97	1.09	1.11	0.97	0.83	0.86	0.84	0.88	0.86	3.79	4.28
Lu	0.26	0.18	0.15	0.20	0.17	0.19	0.19	0.14	0.15	0.15	0.15	0.15	0.15	0.61	0.69
∑REE	239.66	219.46	178.65	231.54	212.61	234.16	250.17	139.24	128.52	129.11	132.28	136.15	132.12	401.94	448.45
δEu	0.90	1.03	1.03	0.99	1.03	1.05	1.04	0.93	1.06	1.03	1.02	1.04	1.03	0.78	0.72
(La/Yb) <sub>N</sub>	21.45	30.09	30.40	27.40	29.48	29.60	31.64	20.24	20.87	20.46	21.11	20.84	20.54	15.97	15.21
T <sub>Zr</sub> (°C)	794	569	585	574	592	572	574	761	592	595	594	597	597	664	658

Chondrite normalized data are taken from McDonough and Sun [55].  $\delta\text{Eu} = \text{Eu}_N / (\text{Sm}_N \times \text{Gd}_N)^{1/2}$ . Calculation of zircon saturation temperatures ( $T_{Zr}$ ) referred to Watson and Harrison [56]. Letter N in footnote means normalize to chondrite.

In Harker diagram (Figure 5), composition of major oxides in the diorite intrusions from both the Yueshan and Zongpu show systematic magmatic evolutionary trend from low  $\text{SiO}_2$  to high  $\text{SiO}_2$ . Contents of  $\text{Fe}_2\text{O}_3$ ,  $\text{TiO}_2$ ,  $\text{CaO}$ ,  $\text{P}_2\text{O}_5$  and  $\text{MgO}$  decrease with increasing of  $\text{SiO}_2$ , suggesting the role of fractional crystallization.  $\text{Na}_2\text{O}$ ,  $\text{K}_2\text{O}$  and  $\text{Al}_2\text{O}_3$  exhibit weak correlations with  $\text{SiO}_2$ .



**Figure 5.** Major element Harker diagrams for diorites and granites in the Anqing orefield. (a)  $\text{Na}_2\text{O}$  vs.  $\text{SiO}_2$ ; (b)  $\text{K}_2\text{O}$  vs.  $\text{SiO}_2$ ; (c)  $\text{MgO}$  vs.  $\text{SiO}_2$ ; (d)  $\text{CaO}$  vs.  $\text{SiO}_2$ ; (e)  $\text{Al}_2\text{O}_3$  vs.  $\text{SiO}_2$ ; (f)  $\text{TiO}_2$  vs.  $\text{SiO}_2$ ; (g)  $\text{P}_2\text{O}_5$  vs.  $\text{SiO}_2$  and (h)  $\text{Fe}_2\text{O}_3$  vs.  $\text{SiO}_2$ .

The REE distribution patterns are similar for the Yueshan and Zongpu diorites (Figure 6a), whereas the Yueshan granites are more enriched in light rare earth elements (LREE) with slightly negative Eu anomalies (Figure 6a). The REE contents of the Yueshan diorites range from 250 ppm to 178 ppm (average 233 ppm), and are slightly higher than those of the Zongpu adakites (average = 133 ppm, ranging from 129 ppm to 139 ppm). No significant Eu anomaly is seen in the Zongpu intrusion, whereas the Yueshan rocks display slightly negative Eu anomalies. Compared to continental crust, the diorites have higher LREE contents and lower heavy rare earth element (HREE) contents. Their REE patterns indicate more fractionation between LREE and HREE relative to continental crust. REE distribution patterns of the Dalongshan granites are shown in Figure 6b, which display clear negative Eu anomalies, and strong fractionation between LREE and HREE with flat HREE patterns. Moreover, these granites have higher REE contents of than those of continental crust and diorites from the Yueshan and Zongpu intrusions. The total REE contents reach up to 449 ppm.

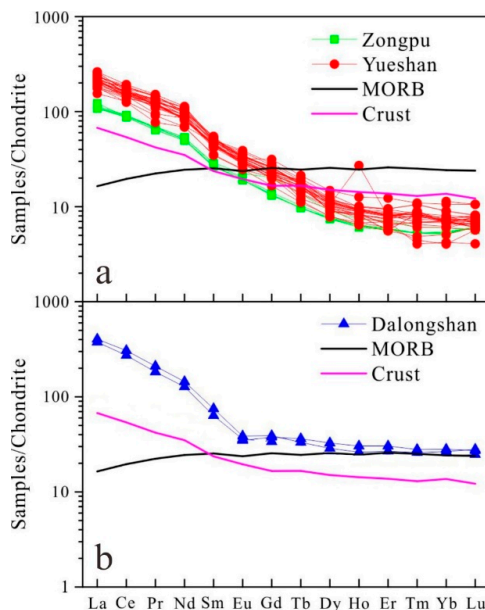


**Figure 6.** Chondrite normalized REE patterns of diorites (a) and granites (b) from the Anqing orefield. Chondrite, MORB and continental crust are taken from [55,57,58], respectively.

The primitive mantle normalized spider diagrams display that the granitoids from the Yueshan, Zongpu and Dalongshan intrusions have similar features of large ion lithophile elements (LILE) enrichment and high field strength elements (HFSE) depletion, in accordance with arc-like signatures (Figure 7). The Yueshan–Zongpu diorites show a similar pattern in their compositions although the Yueshan diorites have higher contents of trace elements than those of the Zongpu. Compared to continental crust, the Yueshan–Zongpu diorites show more enrichment in LILE and LREE. In particular, their Sr and La concentrations are remarkably higher than those of continental crust. The Dalongshan granites show similar patterns with arc-like signature (Figure 7b).

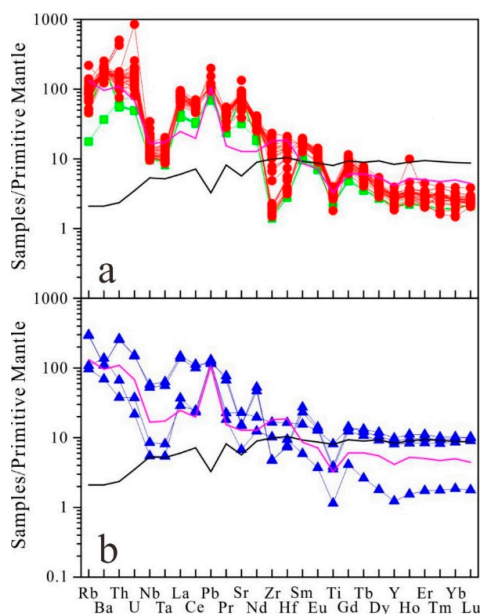


**Figure 7.** Primitive mantle normalized spider diagrams of diorites (a) and granites (b) from the Anqing orefield. Primitive mantle data are taken from [57]. Symbols are as in Figure 4. In addition, the data of two granites from the Dalongshan [49] have been incorporated into Figure 5b.

#### 4.2. Zircon Morphology, U-Pb Dating and Trace Element

Zircon U-Pb isotopic compositions and U-Pb ages of the Yueshan, Zongpu and Dalongshan intrusions from the Anqing orefield are listed in Supplementary data Table S2. Representative zircon CL images, U-Pb concordia diagrams and trace elements are shown in Figure 8. Most of the zircon grains are idiomorphic, with obvious oscillatory zonings, suggesting magmatic origin [59]. Zircons from diorite intrusions show a wide range of uranium and thorium concentrations, with U ranging from 96 ppm to 1768 ppm, Th from 93 ppm to 761 ppm, and Th/U ratios from 0.2 to 1.3, mostly above 0.4. Zircons from the granite intrusion also display a large range with U from 54 ppm to 627 ppm, Th from 65 ppm to 789 ppm, and Th/U ratios ranging from 0.2 to 2.2 (mostly >0.4). Zircons from diorites have higher Th and U contents than those of granites.

The oldest ages are shown by zircon grains in the Zongpu diorite intrusion, with a weighted mean  $^{206}\text{Pb}/^{238}\text{U}$  age of  $138.1 \pm 1.1$  Ma (MSWD = 0.059,  $n = 25$ , 03ZPS02) and  $138.0 \pm 0.8$  Ma (MSWD = 0.46,  $n = 14$ , 14ZP01). Zircons from the Yueshan diorite intrusion show a weighted mean  $^{206}\text{Pb}/^{238}\text{U}$  age of  $136.9 \pm 1.4$  Ma (MSWD = 0.46,  $n = 22$ , 03YS16). The youngest two samples are from the Dalongshan granite intrusion with weighted mean  $^{206}\text{Pb}/^{238}\text{U}$  age  $124.5 \pm 3.6$  Ma (MSWD = 3.1,  $n = 30$ ), and  $124.0 \pm 3.0$  Ma (MSWD = 2.4,  $n = 29$ ). Inherited older zircon grains are rare in our samples. Most of the zircons crystallized from the magmas and the ages can be taken to represent the timing of magma emplacement.

Trace element contents of the zircons are listed in supplementary data Table S3. Chondrite normalized REE diagrams of representative zircons are shown in Figure 8, where they show a similar pattern with positive Ce anomalies, enrichment in HREE and a large range in LREE, in accordance with the features of magmatic zircons [59]. In the Yueshan–Zongpu intrusions, zircon grains in the diorites display slight negative or even no Eu anomalies. However, zircons from the Dalongshan granites show marked negative Eu anomalies (Figure 8). We calculated their zircon Ce(IV)/Ce(III) ratios, and Yueshan zircons have the highest ratios of 300–6000, Zongpu zircons display the relative high and less varied ratios of 300–1000, and Dalongshan zircons show the lowest and wide range of 40–1000 (Figure 14).

Given that most zircons in this study are of magmatic origin, we calculated crystallization temperature using the Ti contents in zircons following by Watson et al. [60]. The results are also listed in Table S3. We chose the peak value of each group of temperature instead of the mathematical average value. The diorites display relatively low crystallization temperatures with a single peak value of 700 °C in the Zongpu and 657 °C in the Yueshan. The Dalongshan granites show higher crystallization temperature than those of the diorites with two peak values at 721 °C and 779 °C.

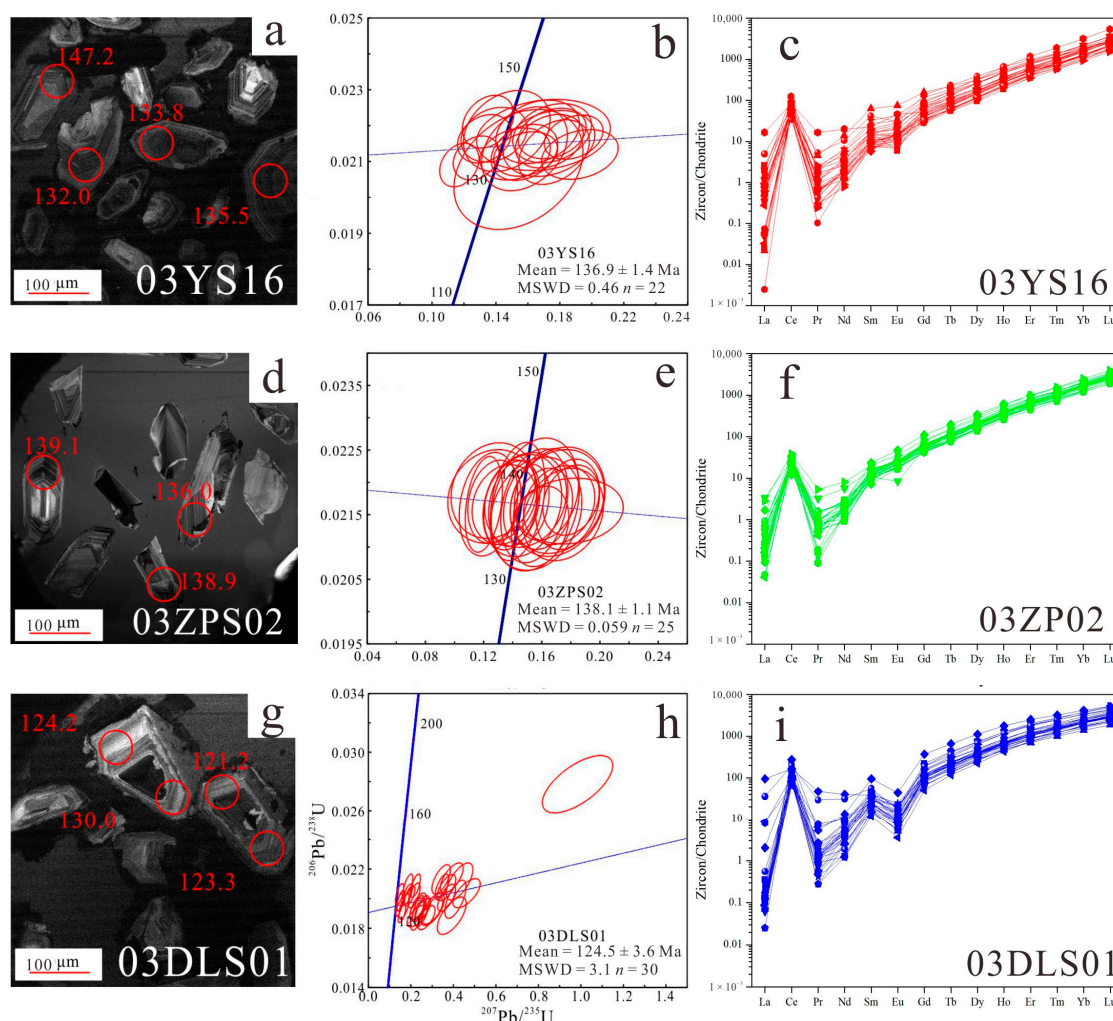


**Figure 8.** CL images, concordia diagrams and REE patterns of zircon grains from the Yueshan (a–c), Zongpu (d–f) and Dalongshan (g–i) intrusions in the Anqing orefield. Chondrite normalized data are taken from [55].

#### 4.3. Zircon Lu-Hf Isotopes

Zircon Lu-Hf isotopic compositions are listed in supplementary data Table S4, and their  $\epsilon_{\text{Hf}}(t)$  value histogram is shown in Figure 9, where the highest frequency is taken to represent the Hf isotopic compositions of the rock. Granitoids from the Anqing orefield show a wide range of  $\epsilon_{\text{Hf}}(t)$ , from the lowest value of  $-23.3$  (03YS16) in the Yueshan diorite intrusion, to the highest value of  $1.5$  (03DLS01) in the Dalongshan granite intrusion. Sample 03DLS03 has  $\epsilon_{\text{Hf}}(t) = -9.5$  with  $T_{\text{DM2}}$  (two-stage Hf model age) at 1793 Ma. Two samples from the Zongpu diorite intrusion share similar Hf isotopic features: one sample (03ZPS02) has  $\epsilon_{\text{Hf}}(t) = -6.8$  with  $T_{\text{DM2}}$  at 1615 Ma, and the other one (14ZP01) has  $\epsilon_{\text{Hf}}(t) = -11.5$  with  $T_{\text{DM2}}$  at 1968 Ma. One sample (03YS16) from the Yueshan diorite intrusion shows the oldest  $T_{\text{DM2}}$  of 2668 Ma.

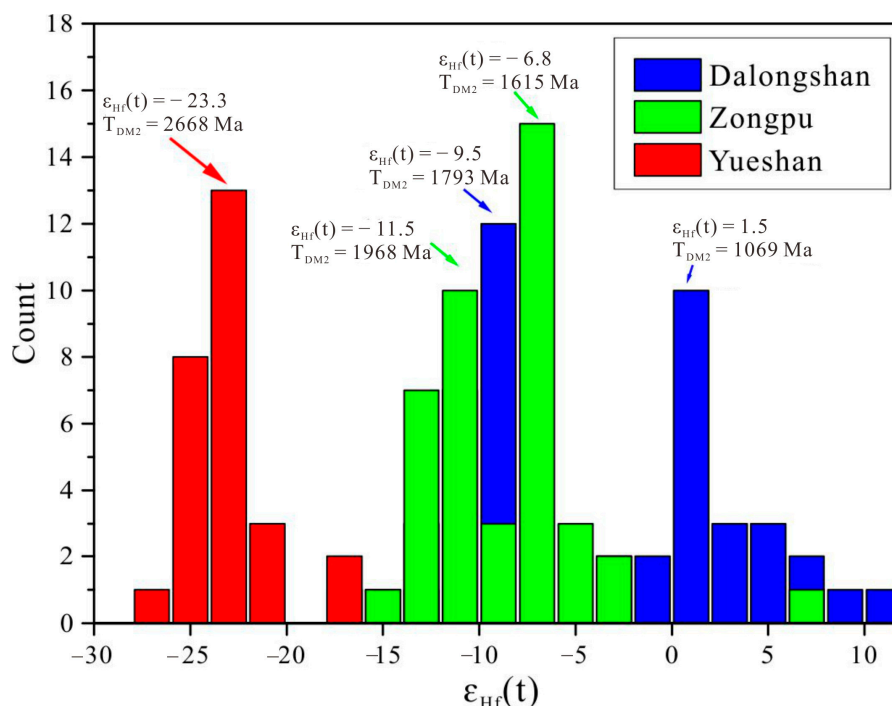


**Figure 9.** Frequency distribution histogram of  $\epsilon_{\text{Hf}}(t)$  values of zircons from granitoids in the Anqing orefield.

## 5. Discussion

### 5.1. Age and Petrogenesis of Diorites

Zircon U-Pb analysis of diorites from the Yueshan–Zongpu intrusions show emplacement ages of 138 Ma to 136 Ma. Our results are consistent with those in a previous study by Chen et al. [61] who obtained an age of 136 Ma by  $^{40}\text{Ar}/^{39}\text{Ar}$  spectra of amphibole from the Yueshan intrusion. Li et al. [62] applied Rb-Sr isochron of the three unaltered minerals (biotite, hornblende and plagioclase) and obtained an age of 137.6 Ma for the Yueshan intrusion. Zhang et al. [33] reported SHRIMP zircon U-Pb age of  $138.7 \pm 0.5$  Ma for diorites in the Yueshan intrusion. The age data from previous studies and our work confirm that the Yueshan intrusion was emplaced at ca. 136 Ma. In the case of Zongpu dioritic intrusion, Wu et al. [63] reported U-Pb zircon age of  $137.5 \pm 2.2$  Ma by LA-ICPMS. This age is also consistent with our result of  $138.1 \pm 1.1$  Ma within uncertainties, suggesting that the dioritic intrusion was emplaced at ca. 138 Ma.

The Yueshan–Zongpu diorites display high Sr (773–2663 ppm) and La (26–54 ppm), with low Y (5.3–16.9 ppm) and Yb (1.7–4.5 ppm). The Sr/Y and (La/Yb)<sub>N</sub> ratios are remarkably high relative to normal island-arc andesites, dacites and rhyolites (ADR) (Figure 10). These, and other geochemical features indicate that the diorites have adakitic affinity [15,17]. The classic adakites defined by Defant and Drummond [15] are characterized by >56 wt %  $\text{SiO}_2$ , >15 wt %  $\text{Al}_2\text{O}_3$ , generally <3 wt %  $\text{MgO}$  (rarely above over 6 wt %), low Y and HREE relative to ADR, high Sr relative to ADR, low HFSE like most of the ADR. Compiling more than 300 adakites analysis, Martin et al. [17] refined this definition and proposed that adakites can be divided into two groups of low- $\text{SiO}_2$  adakites and high- $\text{SiO}_2$  adakites, where the boundary line is 60 wt %. They suggested that HSA are formed by subducted oceanic slab melting, whereas LSA are generated by partial melting of peridotitic mantle wedge.

However, subsequent studies revealed that partial melting of delaminated or thickened lower continental crust can also generate adakitic rocks [3,64]. Thus O-type and C-type adakites were proposed corresponding to oceanic and continental adakites. Figure 11 shows their major differences: C-type has higher  $\text{K}_2\text{O}/\text{Na}_2\text{O}$  than O-type, whereas O-type shows a steeper slope than those of C-type

in the Sr/Y vs. (La/Yb)<sub>N</sub>. Apparently, diorites from the Yueshan and Zongpu intrusions belong O-type adakites (Figure 11). They are also distinct from adakitic rocks formed by the melting of thickened lower continental crust.

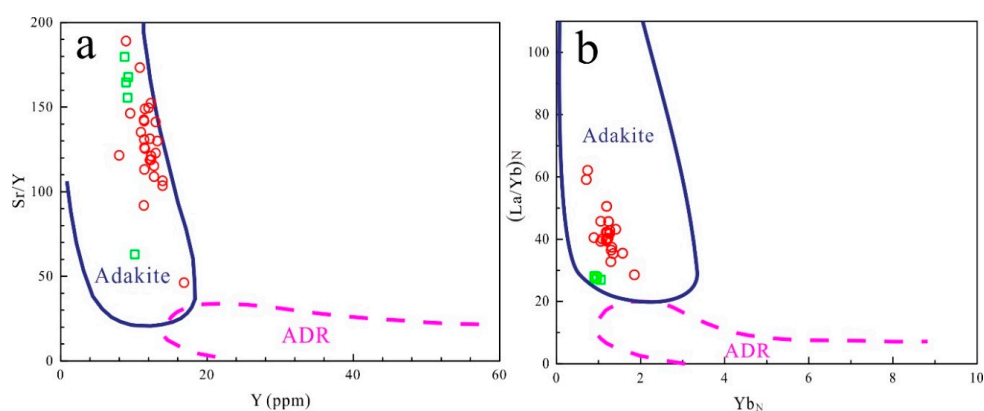


**Figure 10.** Classification diagrams of (a) Sr/Y vs. Y and (b) (La/Yb)<sub>N</sub> vs. Yb<sub>N</sub> for diorites from the Yueshan and Zongpu after [15]. ADR: normal andesites, dacites and rhyolites. The boundaries between ADR and adakite are taken from [65]. Symbols are as in Figure 4.

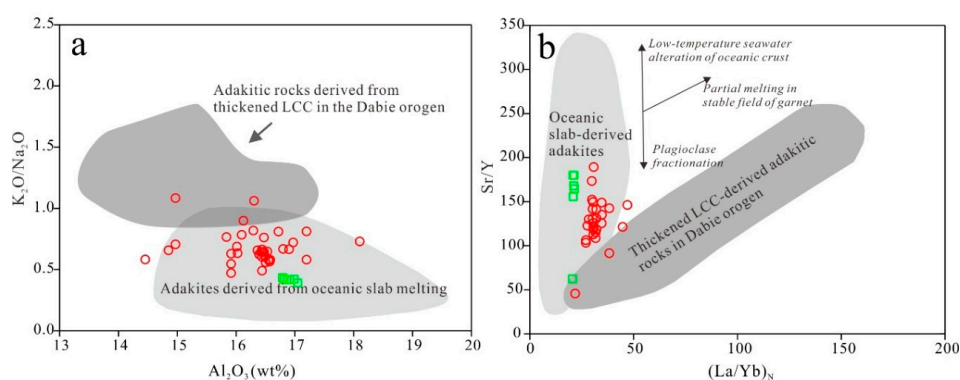


**Figure 11.** (a) K<sub>2</sub>O/Na<sub>2</sub>O vs. Al<sub>2</sub>O<sub>3</sub> diagram comparing adakites from the Yueshan–Zongpu and other localities. Field of oceanic slab-derived adakites is after [66]; whereas field of Dabie adakites from thickened LCC (lower continental crust) is from [30]; (b) Sr/Y vs. (La/Yb)<sub>N</sub> diagram for the Yueshan–Zongpu intrusive rocks. Modified after [30]. Symbols are as in Figure 4.

Most adakites from the Yueshan and all from Zongpu have SiO<sub>2</sub> contents <60 wt % and >60 wt %, respectively. Thus we classify that the Yueshan adakites as LSA and the Zongpu adakites as HSA. The two groups adakites show marked differences in their major and trace element compositions (Figure 12), suggesting distinct sources for their petrogenesis. The LSA differ from HSA primarily in that they have lower silica contents but higher MgO contents (Figure 12a). Niobium, as an important high field strength element (HFSE) and immobile element, its contents in LSA are systematical higher than the HSA [17], which is evidenced by this present (Figure 12b). In the Figure 12c, both K and Rb displayed significant differences between LSA and HSA. Although most Yueshan adakites located out of the field of LSA, they have similar geochemical features of lower K and Rb contents to LSA. The Yueshan adakites have the lower Cr/Ni ratios and narrow range in contrast with the Zongpu adakites (Figure 12d), indicating a source that is not basaltic, but mantle peridotite melting [17]. The HSA mainly formed from the direct melting of subducted oceanic slab, variably contaminated by slab-melts; whereas the LSA were generated by melting of a peridotitic mantle wedge whose composition has been modified by reaction with felsic slab-melts [17].

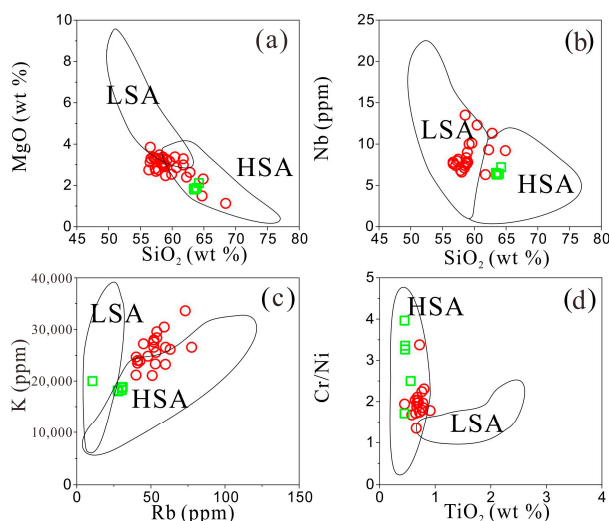


**Figure 12.** Comparison of HSA and LSA. Ranges of HSA and LSA are taken from [17]. (a) MgO vs. SiO<sub>2</sub>; (b) Nb vs. SiO<sub>2</sub>; (c) K vs. Rb; (d) Cr/Ni vs. TiO<sub>2</sub>. Symbols are as in Figure 4.

Porphyry copper-gold deposits are widely distributed within the LYRB (Figure 1), which are regarded to be closely related to the adakitic intrusions. Their petrogenesis remains controversial, with diverse models proposed including: (1) partial melting of subducted oceanic crust [4,30] or ridge subduction [7,22]; (2) partial melting of thickened or delaminated lower continental crust [3,64,67]; and (3) mixing of enriched mantle-derived and lower crust-derived magmas [11,13]. The Yueshan and Zongpu adakites show higher  $\epsilon_{\text{Nd}}(t)$  values than those of the thickened Yangtze lower crust and the adakites from this (Figure 13). They also display higher MgO contents than those of lower crust-derived adakites (Table 1 [28]). Moreover, the  $f\text{O}_2$  of such adakites are too low to generate the porphyry copper-gold deposits in the LYRB. In this study, the zircon Ce(IV)/Ce(III) and  $\delta\text{Eu}$ , apparently suggest high  $f\text{O}_2$  environment (Figure 14). The melts derived from delaminated lower crust will be characterized by elevated Cr and Ni contents due to reaction of melt-peridotite during their ascend [68]. However, neither the Yueshan nor Zongpu adakites have high Cr and Ni contents (Cr: 25–63 ppm, Ni: 13–17 ppm, Table 1). Thus, this model is excluded.

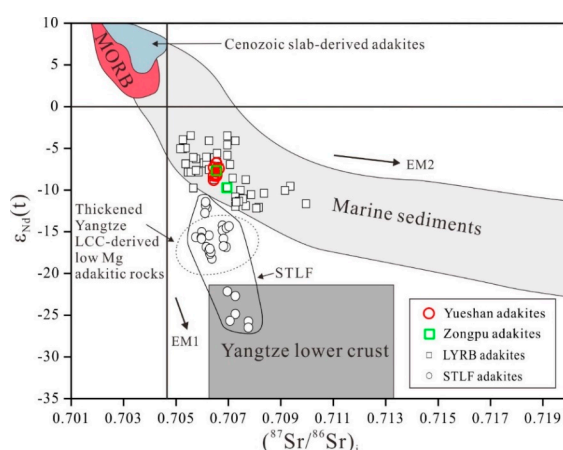


**Figure 13.** Initial Sr-Nd isotopes of the Yueshan and Zongpu adakites from the Anqing orefield (data sourced from [28,32,69]; diagram modified after from [30]). Data sources: Cenozoic slab-derived adakites [70], thickened Yangtze lower crust-derived low-Mg adakitic rocks [71–73], LYRB and STLFF (South Tan-Lu Fault) adakites [28,30], and the early Cretaceous mafic igneous rocks in the LYRB [74]; MORB and marine sediments [75]; Yangtze lower crust [76].

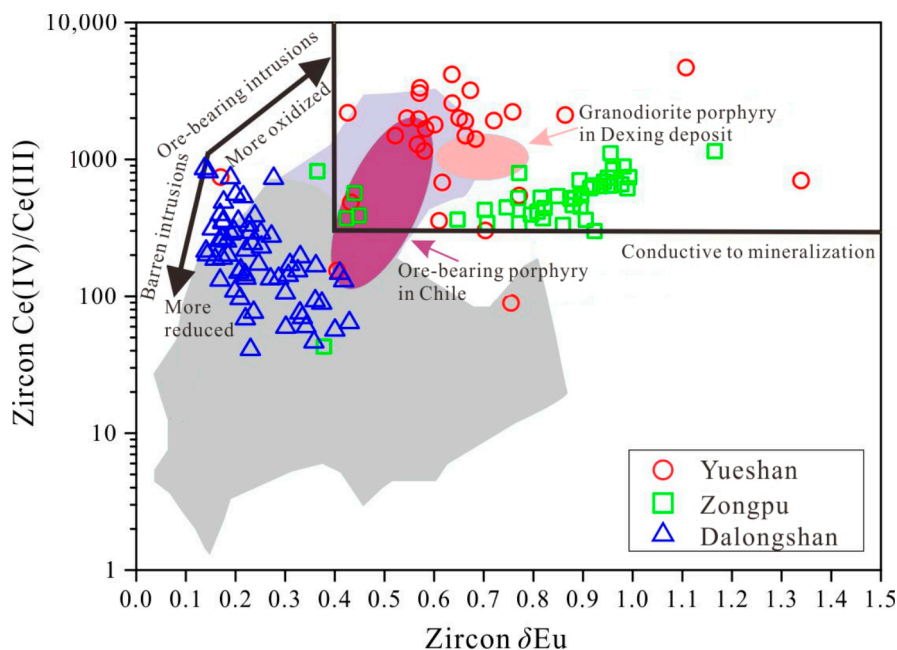


**Figure 14.** Ce(IV)/Ce(III) vs.  $\delta\text{Eu}$  oxygen fugacity discrimination diagram of zircons from adakites and granites in the Anqing orefield. Background data are referred to [77,78].

Previous studies have argued against a subduction-related petrogenesis on the basis of highly enriched Nd and Hf isotopes relative to MORB and Cenozoic slab-derived adakites (Figures 13 and 15). The isotopic investigations on the early Cretaceous mafic volcanic rocks from Ningzhen and Ningwu regions in the LYRB demonstrate the presence of enriched lithospheric mantle instead of depleted mantle or primitive mantle [74]. The field of Sr-Nd isotopes for felsic adakites overlaps with the composition of mafic/basaltic volcanic rocks, and their relationship seems to be more likely related to Cenozoic slab-derived adakites and MORB (Figures 11 and 13 in [30]; Figure 11 in [12]). The enriched lithospheric mantle resulted through interaction between the mantle and the Paleo-Pacific plate, resulting in upwelling of asthenosphere or Neoproterozoic subducted material [79], or were generated from the oceanic slab subduction during collision of the Yangtze and Cathaysia blocks [80]. Thus ancient continental materials must be involved during the enriched lithospheric mantle formation, as also confirmed by the presence of Neoproterozoic inherited zircons (Figure 15 [63]).

Although the HSA and LSA share similar trace elemental features, they display significant differences in major element and isotopic compositions. Magma mixing of enriched mantle- and lower crust-derived melts lead to a mixture between two endmembers. However, neither isotopic nor elemental (concentrations and ratios) show any linear or hyperbolic relationship (e.g., Figure 13). Moreover, considerable amounts of LYRB adakites fall far from the mixing line in the Sr-Nd isotopic diagram (Figure 13). Plagioclases from the Shaxi adakites within the LYRB do not show any zoning, which also argues against magma mixing process [12]. Coeval HSA and LSA are more likely to have formed in subduction-related setting [17]. In the LYRB, enriched sub-arc mantle wedge metasomated by slab-melts or slab-fluids resulted in the adakitic signatures, followed by partial melting which produced the LSA with enriched Nd-Hf isotopic compositions (Figures 13 and 15). The HSA formed by subducted slab melting and melt-peridotite interaction during ascent through mantle wedge. Therefore, partial melting of subducted oceanic slab and hydrated enriched mantle wedge are considered as the possible scenario for the petrogenesis of LSA and HSA.

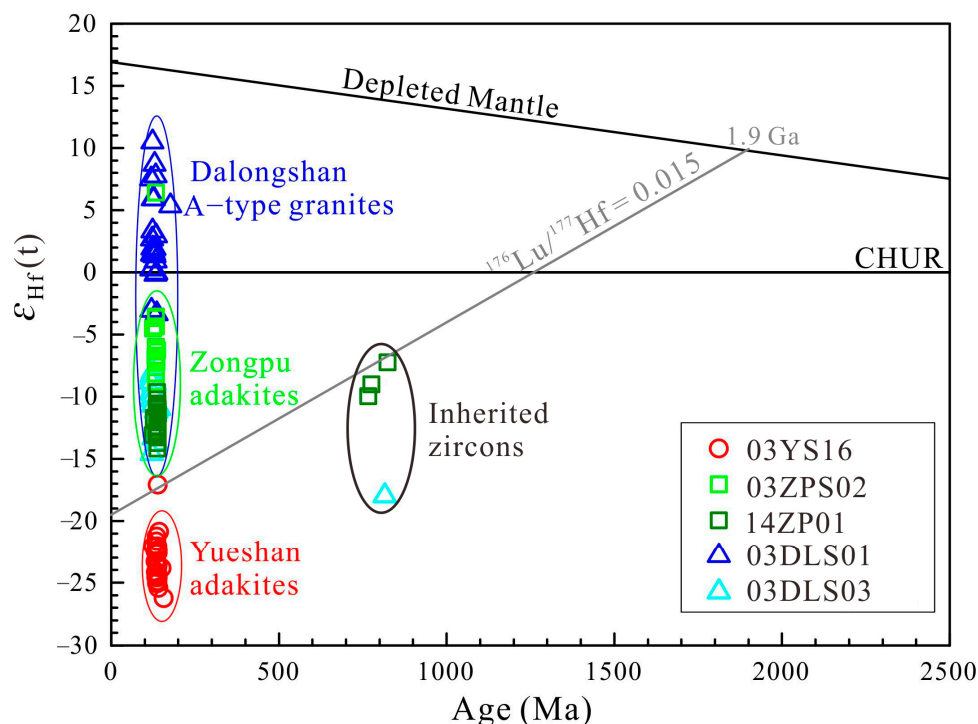


**Figure 15.** Zircon  $\epsilon_{\text{Hf}}(t)$  values vs.  $^{206}\text{Pb}/^{238}\text{U}$  ages diagram for the Yueshan-Zongpu adakites and the Dalongshan granites in the Anqing orefield. Depleted mantle and CHUR (chondrite uniform reservoir) have been defined in Section 3.3.

## 5.2. Age and Petrogenesis of A-Type Granites

Two A-type granite belts are distributed parallel in the northern and southern domains of the Yangtze River. These granites are rich in alkali (high up to 12 wt %), poor in water (low only about 0.5 wt %) and show very high  $10,000 \times \text{Ga}/\text{Al}$  ratios. The Dalongshan A-type granites belong to the northern belt, composed of syenite, quartz syenite and alkali-feldspar granite with ages in the range of 128–124 Ma [47,79]. In this study, the Dalongshan A-type granites yield an age of 124 Ma (Figure 8), in accordance with previous results within error [49,81].

A-type granites are characterized by high  $\text{Fe}/(\text{Fe} + \text{Mg})$  and  $\text{K}_2\text{O}/\text{Na}_2\text{O}$  ratios, and incompatible elements contents compatible with mafic silicates (e.g., Co, Sc, Cr and Ni) and feldspars (e.g., Ba, Sr, Eu) [20]. In this study, the Dalongshan granites are enriched in LILE (Rb, Th, U, REE except Eu) and HFSE (Zr, Hf, Nb and Ta), and show high total alkali ( $\text{K}_2\text{O} + \text{Na}_2\text{O}$ ) (8.6 wt %–11.2 wt %) with high  $\text{K}_2\text{O}/\text{Na}_2\text{O}$  ratios of 0.9, in accordance with typical A-type granites. Furthermore, calculated Ti-in-zircon temperatures (based on equation of [60]) for two granite samples are in the range of 672 °C to 837 °C with an average of 748 °C, implying a relatively high temperature origin. Since trace elements could be easily affected by crystal fractionation, Frost et al. [82] proposed a new geochemical classification for granitic rocks by introducing two parameters: modified alkali-lime index (MALI,  $\text{Na}_2\text{O} + \text{K}_2\text{O} - \text{CaO}$ ) for feldspars abundance which is related to magma origin, and  $\text{FeOT}/(\text{FeOT} + \text{MgO})$  for information from crystal fractionation of granitoid magma (Figure S1). These diagrams show that the Dalongshan granites belong to alkali- and ferroan- A-type granites (Figure S1). A-type granites have been further divided into A1 and A2 chemical subgroups [21]. The A1 subgroup is characterized by elemental ratios similar to those of oceanic-island basalts (OIB), whereas A2 subgroup is characterized by elemental ratios that vary from those of continental crust to those of island-arc basalts (IAB). It is proposed that two sub-types have different sources and tectonic settings [21]. Based on discrimination diagrams in Figure 16, the Dalongshan granites are located within the field of A1-type granites, which represent differentiates of magmas derived from OIB-like

basalts emplaced in continental rifts during intraplate magmatism. The A1-type granites suggest an intraplate extensional tectonic setting, in contrast to the Yueshan–Zongpu coeval HSA and LSA reflecting a subduction-related setting.

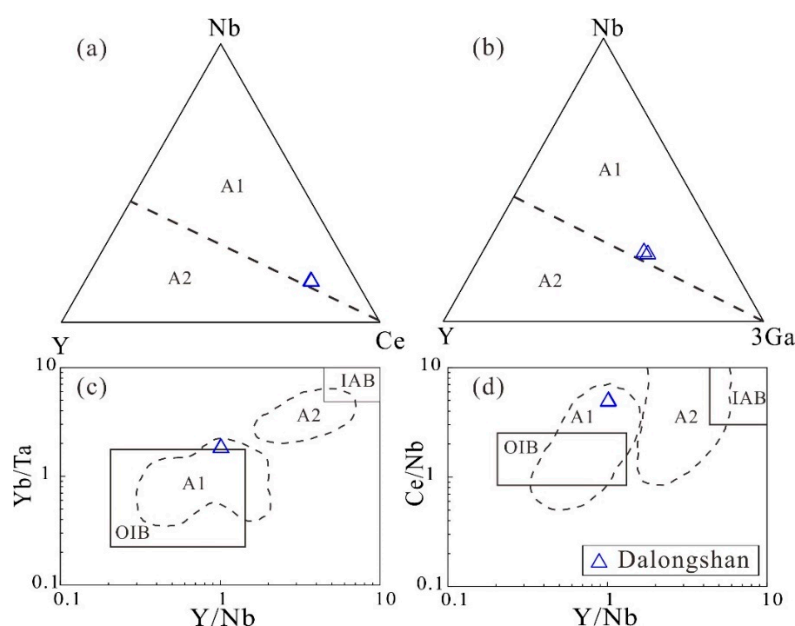


**Figure 16.** Discrimination diagrams of A-type granites. (a–d) are modified from [20,82,83], respectively.

The petrogenesis of A-type granites remains controversial, and diverse scenarios have been proposed as follow: (1) combined crustal and mantle sources, in the form of either crustal assimilation and fractional crystallization of mantle-derived magmas, or mixing between mantle- and crust- derived magmas [24]; (2) Anatexis of continental crustal protoliths that were previously depleted by extraction of a hydrous felsic melts [20]; (3) Extreme differentiation of mantle-derived tholeiitic or alkaline magma precursor [84]. A-type granites with ages of 130–124 Ma are widely distributed in the LYRB, and include the Huangmeijian, Tongshan, Damaoshan and Yangshan intrusions. Wong et al. [85] suggested that the Baijuhuajian A-type granites were derived from a predominantly mantle component followed by extensive crystal fractionation with minor input of older crustal materials. However, the enriched Nd–Hf isotopes argue strongly against this interpretation due to lack of juvenile crust materials as the dominant source [14]. On the other hand, Jiang et al. [86] proposed that the Tongshan and Damaoshan A-type granites formed by partial melting of Mesoproterozoic source rock involving both metasedimentary and metaigneous rocks that were previously depleted by extraction of a felsic melt. The Dalongshan granites show marked variation of zircon  $\varepsilon_{\text{Hf}}(t)$  values ranging from  $-18$  to  $10.5$  with an average of  $-3.9$  (Figure 15). The corresponding peaks  $T_{\text{DM2}}$  are 1793 Ma and 1069 Ma, respectively (Figure 9). Furthermore, they have high  $\text{SiO}_2$  contents of about 64 wt % (Table 1), implying that they are unlikely to have been sourced directly from the mantle, even from a metasomatized and enriched mantle. Thus a possible source for the A-type granites in this area is either Mesoproterozoic crust or Neoproterozoic crust. Previous zircon Hf isotope data from magmatic and basement metamorphic rocks in the Yangtze Block suggest three episodes of crustal growth at 3.8–3.6 Ga, 2.6–2.5 Ga and 1.2–0.8 Ga [10,79], among which the Neoproterozoic crust might be the likely source. The presence of positive zircon  $\varepsilon_{\text{Hf}}(t)$  values implies minor input of juvenile components. The subducted slab break off at about 124 Ma resulted in, asthenosphere upwelling and formation of mafic magmas. The ascent of these magma and melting of the overlying Neoproterozoic crust produce the Dalongshan A-type granites, as illustrated in a petrogenetic model in Figure 17. The other petrotectonic model involved slab subduction and roll-back [10], which could account for the minor juvenile input. In their model, the lithospheric mantle had been metasomatized by fluid/melt from a subducted slab, and especially

from the slab sediments before 148 Ma [10]. The slight differences between their model and our model, are that the subducted time in this region is exactly constrained at 138 Ma. The subducted products are evidenced by HSA and LSA as illustrated in Figure 17a.

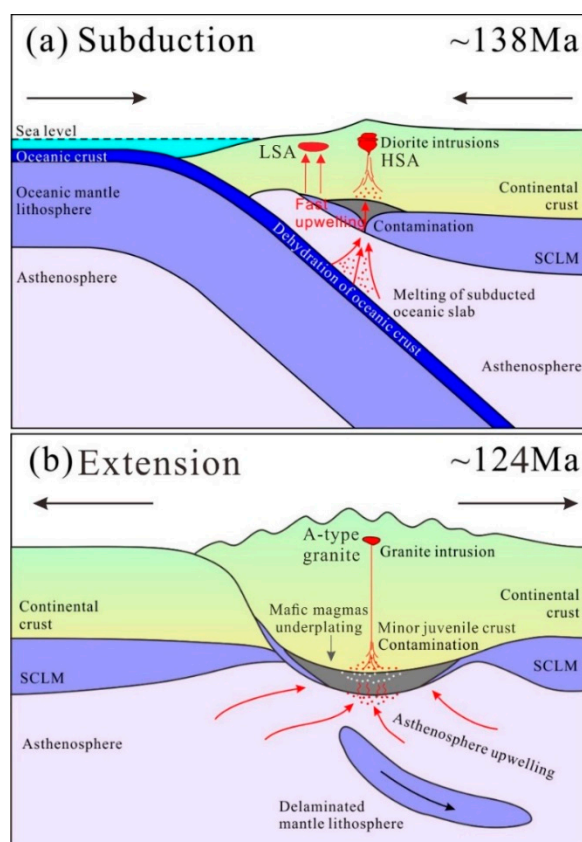


**Figure 17.** Schematic geodynamic model showing the petrogenesis of the Yueshan-Zongpu adakites and the Dalongshan A-type granites in the Anqing orefield during 138–124 Ma. (a) the subducted model, and (b) the delamination model, reproduced with permission from Richards [87,88], published by Geological Society of America and Elsevier, respectively; modified with concepts from [3,10]. See text for discussion. SCLM, subcontinental lithospheric mantle.

### 5.3. Tectonic Evolution and Mineralization

The LYRB in eastern China is an important metallogenic belt, which is closely associated with and genetically related to the late Mesozoic magmatic rocks [1,2,10,11]. Three major magmatic pulses are identified in this region: (1) first stage at 148–133 Ma, represented by intermediate to felsic calc-alkaline intrusions associated with Cu-Au-Mo polymetallic deposits [11,89]; (2) mafic to intermediate alkaline volcanic and subvolcanic rocks associated with magnetite-apatite deposits representing the second stage at 133–127 Ma [11,89]; and (3) A-type granites linked to uranium and gold mineralization in the third stage (127–123 Ma) [10]. This study involved the first and third stages, corresponding to adakites and A-type granites.

In the first stage, the Paleo-Pacific subducted slab dehydrates and leading to partial melting of oceanic crust, and producing slab-melts. The melts interacted with peridotites in the mantle wedge, and generate the HSA. Since the depth of formation of slab-melts are greater than those for the formation of LSA, the magmas temperatures should be higher than those of LSA. This is consistent with our results that show Ti-in-zircon temperatures for the Zongpu HSA as 738 °C, but only 656 °C for the Yueshan LSA (Table S3). Following this, the ascending slab-melts metasomatized the overlying enriched mantle wedge and triggered partial melting, producing the LSA. In this scenario,

the formation age of LSA should be slightly younger than those of HSA. The Yueshan LSA (136 Ma) shows systematically younger age than that of the Zongpu HSA (138 Ma). This feature is also confirmed by the Shujiadian quartz diorite porphyry (143.7 Ma) in contrast to the pyroxene diorite (139.8 Ma) [13] as well as the Shaxi quartz diorite (130 Ma) as against the biotite-gabbro (129 Ma) [12].

Under subduction-related setting, fluids released from the oceanic slab enrich the magma source with S, H<sub>2</sub>O, and metals [77], which also provides high  $fO_2$  (QFM + 2 [90]). This is confirmed by the zircon Ce(IV)/Ce(III) vs.  $\delta Eu$  oxygen fugacity discrimination diagram (Figure 14), indicating high magmatic oxidation state [77]. Ce(IV)/Ce(III) ratio within zircon can be calculated using a lattice-strain model for mineral-melt partitioning of Ce(IV) and Ce(III), in combination with zircon  $\delta Eu$  values, magmatic oxidation states can be inferred [77]. High oxygen fugacity may eliminate sulfides in the source region and keep the melt sulfide under-saturated, thereby promoting porphyry copper mineralization [12,91]. The other important factor is that oceanic crust has higher initial Cu contents than those of continental crust and mantle [92], thus subducted oceanic slab is a favorable source for Cu. In this study, the Dalongshan granites are plotted in the field of barren intrusions with low oxygen fugacity, whereas the Yueshan–Zongpu adakites fall within field of ore-bearing host rocks with high  $fO_2$ . This is the possible reason for the concentration of porphyry Cu deposits in the Yueshan–Zongpu intrusions (Figure 1).

In the third stage, accompanying roll-back of the subducted slab, more intense extension allowed upwelling of the asthenosphere, destruction of the lithospheric mantle, and reworking of the Neoproterozoic crust during 127–123 Ma [10]. Sun et al. [22] proposed a marked change in the drift direction of the Paleo-Pacific plate during this period, and correlated this with the formation of gold mineralization in eastern China. The coeval A-type granites in LYRB are controlled by the northwestward subduction of the Paleo-Pacific plate as inferred from: (1) the NE-striking of the Yangtze Block; and (2) the NE-SW elongation of most granites in the LYRB [14]. The continental arc setting has been identified by the coeval diabasic dyke [86], and the regional geological characteristics suggest that A-type granites are probably emplaced at the beginning of back-arc extension. The underplating of mafic magmas triggered partial melting of Mesoproterozoic–Neoproterozoic crust in the back-arc extension regime, in response to the drift direction of the Paleo-Pacific plate, producing A-type granites in LYRB [14]. In summary, the LSA and HSA together with A-type granites record a tectonic transition from a compressive to an extensional setting during 138–124 Ma. In a short time of 14 Ma, the tectonic transition can be occurred. In Sabzevar structural zone (NE Iran), the extensional regime and the magmatic flare-up (45 Ma) [93] is 13 Ma younger than high-pressure pristine adakitic slab melts (ca. 58 Ma) intruded in the subduction channel [94]. Both well-documented examples from the Anqing area and the Sabzevar structural zone confirmed that tectonic transition from a compressive to an extensional setting could happen in a short time, e.g., 14 Ma.

The Dalongshan A-type granites formed by anatexis of uranium-rich Precambrian metasedimentary rocks. Deuteric alteration of primary U-bearing accessory minerals such as zircon, titanite and apatite, and the erosion of the granites under a hot, dry paleoclimate lead to partial release of U [95]. Uranium is hosted in pitchblende along tectonic fractures, and interstitially fill the granular minerals. Late Yanshanian magmatic event at 124 Ma as well as radioactive decay of K, U in the A type-granite provided additional heat source for the formation of U-bearing hydrothermal fluids. Crystal fractionation of K-feldspar and biotite during the formation of A-type granites resulted in relative enrichment in Si, U and HREE (Figure 6), further providing a potential U enriched source. The other U source in the area is sandstone, which has high U content (21 ppm) [96]. Hydrothermal alteration can further concentrate the U contents in altered sandstone and A-type granites, which comprise pre-ore alkali-metasomatism and ore-stage hydrothermal chloritization, pyritization, hematitization, silicification, damouritization and carbonatization. The ore-forming temperature of the Dalongshan U deposit has been constrained at 270–290 °C, and the time of major ore formation is dated at 110 Ma, belonging to the mesothermal to epithermal U deposit [96].

## 6. Conclusions

- (1) Adakites from the Anqing orefield can be divided into two groups as LSA and HSA, corresponding with the Yueshan and Zongpu diorites, respectively. Subduction-related setting is proposed for the magma genesis and involved the following processes. In the early stage, the HSA formed by slab-melts that reacted with peridotite during ascend through the overlying enriched mantle wedge. Subsequently, melting of a peridotitic overlying enriched mantle wedge whose composition has been modified by reaction with slab-melts occurred. Zircons in the HSA and LSA yield ages of 138 Ma and 136 Ma, respectively. Porphyry copper-gold deposits are closely associated with and genetically related to these adakites.
- (2) The A1-type granites are dated at 124 Ma, and their zircon  $\epsilon_{\text{Hf}}(t)$  values and geochemical features suggest formation through partial melting of Neoproterozoic crust with minor juvenile input under a back-arc extensional setting associated with the roll-back of Paleo-Pacific plate. The source for U in the associated ore deposit is considered to be the A-type granites and sandstones. The emplacement of A-type granitic intrusion provided the heat and fluids which mobilized and concentrated the U.
- (3) The adakites together with A-type granites record a tectonic transition from a compressive to an extensional setting during 138–124 Ma.

**Supplementary Materials:** The following are available online at <http://www.mdpi.com/2075-163X/8/8/328/s1>, Figure S1: Discrimination diagrams of A-type granites (modified after [82]), Table S1: Published data for major and trace element compositions of the Yueshan, Zongpu and Dalongshan intrusions in the Anqing orefield, Table S2: Zircon LA-ICPMS U-Pb data for granitoids in the Anqing orefield, Table S3: Trace element compositions of zircons (ppm) from granitoids in the Anqing orefield, Table S4: Lu-Hf isotope analysis results of zircons from granitoids in the Anqing orefield.

**Author Contributions:** Conceptualization, L.L. and G.C.; Methodology, Q.H.; Validation, X.Y.; Formal Analysis, Y.L.; Investigation, L.L.; Resources, X.Y.; Data Curation, G.C.; Writing: Original Draft Preparation, L.L. and G.C.; Writing: Review and Editing, M.S.; Supervision, X.Y.; Project Administration, X.Y.; Funding Acquisition, X.Y.

**Funding:** This study is supported by MOST of China (No. 2016YFC0600404), the Natural Science Foundation of China (Grant Nos. 41173057, 41372087 and 41090372), and Project of Geological Science and Technology of Anhui Province (2014-K-04).

**Acknowledgments:** The authors are grateful to two anonymous reviewers and Assistant Editor Jelena Milojevic for their helpful comments and suggestions that greatly helped to improve an earlier manuscript version. We appreciate H. Zhang, M.L. Dai, Z.H. Hou, M. Xia, J.H. Deng, H.L. Gu, H.S. Qi, Y.S. Ren, X. Zhang, S.Y. Shu, and Q. Hu for assistance in zircon U-Pb dating and Lu-Hf isotope analyses. Finally, we greatly thank Z.X. Nie and L. Shi for field assistance.

**Conflicts of Interest:** The authors declare no conflict of interest.

## References

1. Chang, Y.F.; Liu, X.P.; Wu, C.Y. *The Copper-Iron Belt of the Lower and Middle Reaches of the Changjiang River*; Geological Publishing House Press: Beijing, China, 1991; pp. 1–234, (In Chinese with English Abstract).
2. Pan, Y.M.; Dong, P. The Lower Changjiang (Yangzi/Yangtze River) metallogenic belt, east central China: Intrusion- and wall rock-hosted Cu-Fe-Au, Mo, Zn, Pb, Ag deposits. *Ore Geol. Rev.* **1999**, *15*, 177–242. [[CrossRef](#)]
3. Wang, Q.; Wyman, D.A.; Xu, J.F.; Zhao, Z.H.; Jian, P.; Xiong, X.L.; Bao, Z.; Li, C.; Bai, Z. Petrogenesis of Cretaceous adakitic and shoshonitic igneous rocks in the Luzong area, Anhui Province (Eastern China): Implications for geodynamics and Cu-Au mineralization. *Lithos* **2006**, *89*, 424–446. [[CrossRef](#)]
4. Ling, M.X.; Wang, F.Y.; Yang, X.Y.; Sun, W.D. Cretaceous magmatism along the Lower Yangtze River, China controlled by ridge subduction. *Geochim. Et Cosmochim. Acta* **2008**, *72*, A554.
5. Xie, G.Q.; Mao, J.W.; Li, X.W.; Duan, C.; Yao, L. Late Mesozoic bimodal volcanic rocks in the Jinniu basin, Middle-Lower Yangtze River Belt (YRB), East China: Age, petrogenesis and tectonic implications. *Lithos* **2011**, *127*, 144–164. [[CrossRef](#)]

6. Xie, J.C.; Yang, X.Y.; Sun, W.D.; Du, J.G. Early Cretaceous dioritic rocks in the Tongling region, eastern China: Implications for the tectonic settings. *Lithos* **2012**, *150*, 49–61. [[CrossRef](#)]
7. Sun, W.D.; Ling, M.; Chung, S.; Ding, X.; Yang, X.; Liang, H.; Fan, W.; Goldfarb, R.; Yin, Q. Geochemical Constraints on Adakites of Different Origins and Copper Mineralization. *J. Geol.* **2012**, *120*, 105–120. [[CrossRef](#)]
8. Li, X.H.; Li, Z.; Li, W.; Wang, X.; Gao, Y. Revisiting the “C-type adakites” of the Lower Yangtze River Belt, central eastern China: In-situ zircon Hf-O isotope and geochemical constraints. *Chem. Geol.* **2013**, *345*, 1–15. [[CrossRef](#)]
9. Wang, F.Y.; Liu, S.; Li, S.; Akhtar, S.; He, Y. Zircon U-Pb ages, Hf-O isotopes and trace elements of Mesozoic high Sr/Y porphyries from Ningzhen, eastern China: Constraints on their petrogenesis, tectonic implications and Cu mineralization. *Lithos* **2014**, *200*, 299–316. [[CrossRef](#)]
10. Yan, J.; Liu, J.; Li, Q.; Xing, G.; Liu, X.; Xie, J.; Chu, X.; Chen, Z. In situ zircon Hf-O isotopic analyses of late Mesozoic magmatic rocks in the Lower Yangtze River Belt, Central Eastern China: Implications for petrogenesis and geodynamic evolution. *Lithos* **2015**, *227*, 57–76. [[CrossRef](#)]
11. Zhou, T.F.; Wang, S.; Fan, Y.; Yuan, F.; Zhang, D.; White, N. A review of the intracontinental porphyry deposits in the Middle-Lower Yangtze River Valley metallogenic belt, Eastern China. *Ore Geol. Rev.* **2015**, *65*, 433–456. [[CrossRef](#)]
12. Deng, J.H.; Yang, X.; Li, S.; Gu, H.; Mastoi, A.; Sun, W. Partial melting of subducted paleo-Pacific plate during the early Cretaceous: Constraint from adakitic rocks in the Shaxi porphyry Cu-Au deposit, Lower Yangtze River Belt. *Lithos* **2016**, *262*, 651–667. [[CrossRef](#)]
13. Wang, S.W.; Zhou, T.; Yuan, F.; Fan, Y.; Cooke, D.; Zhang, L.; Fu, B.; White, N. Geochemical characteristics of the Shujiadian Cu deposit related intrusion in Tongling: Petrogenesis and implications for the formation of porphyry Cu systems in the Middle-Lower Yangtze River Valley metallogenic belt, eastern China. *Lithos* **2016**, *252*, 185–199. [[CrossRef](#)]
14. Gu, H.L.; Yang, X.; Deng, J.; Duan, L.; Liu, L. Geochemical and zircon U-Pb geochronological study of the Yangshan A-type granite: Insights into the geological evolution in south Anhui, Eastern Jiangnan Orogen. *Lithos* **2017**, *284*, 156–170. [[CrossRef](#)]
15. Defant, M.J.; Drummond, M.S. Derivation of Some Modern Arc Magmas by Melting of Young Subducted Lithosphere. *Nature* **1990**, *347*, 662–665. [[CrossRef](#)]
16. Kay, R.W. Aleutian Magnesian Andesites—Melts From Subducted Pacific Ocean Crust. *J. Volcanol. Geotherm. Res.* **1978**, *4*, 117–132. [[CrossRef](#)]
17. Martin, H.; Smithies, R.; Rapp, R.; Moyen, J.; Champion, D. An overview of adakite, tonalite-trondhjemite-granodiorite (TTG), and sanukitoid: Relationships and some implications for crustal evolution. *Lithos* **2005**, *79*, 1–24. [[CrossRef](#)]
18. Zhang, Q.; Wang, Y.; Qian, Q.; Yang, J.; Wang, Y.; Zhao, T.; Guo, G. The characteristics and tectonic-metallogenic significance of the adakites in Yanshan period from eastern China. *Acta Petrol. Sin.* **2001**, *17*, 236–244, (In Chinese with English Abstract).
19. Chung, S.L.; Liu, D.; Ji, J.; Chu, M.; Lee, H.; Wen, D.; Lo, C.; Lee, T.; Qian, Q.; Zhang, Q. Adakites from continental collision zones: Melting of thickened lower crust beneath southern Tibet. *Geology* **2003**, *31*, 1021–1024. [[CrossRef](#)]
20. Whalen, J.B.; Currie, K.L.; Chappell, B.W. A-Type Granites—Geochemical Characteristics, Discrimination and Petrogenesis. *Contrib. Mineral. Petrol.* **1987**, *95*, 407–419. [[CrossRef](#)]
21. Eby, G.N. Chemical Subdivision of the a-Type Granitoids—Petrogenetic and Tectonic Implications. *Geology* **1992**, *20*, 641–644. [[CrossRef](#)]
22. Sun, W.D.; Ding, X.; Hu, Y.; Li, X. The golden transformation of the Cretaceous plate subduction in the west Pacific. *Earth Planet. Sci. Lett.* **2007**, *262*, 533–542. [[CrossRef](#)]
23. Mao, J.R.; Li, Z.L.; Ye, H.M. Mesozoic tectono-magmatic activities in South China: Retrospect and prospect. *Sci. China Earth Sci.* **2014**, *57*, 2853–2877. [[CrossRef](#)]
24. Yang, J.H.; Wu, F.; Chung, S.; Wilde, S.; Chu, M. A hybrid origin for the Qianshan A-type granite, northeast China: Geochemical and Sr-Nd-Hf isotopic evidence. *Lithos* **2006**, *89*, 89–106. [[CrossRef](#)]
25. Douce, A.E.P. Generation of metaluminous A-type granites by low-pressure melting of calc-alkaline granitoids. *Geology* **1997**, *25*, 743–746. [[CrossRef](#)]

26. Mingram, B.; Trumbull, R.; Littman, S.; Gerstenberger, H. A petrogenetic study of anorogenic felsic magmatism in the Cretaceous Paresis ring complex, Namibia: Evidence for mixing of crust and mantle-derived components. *Lithos* **2000**, *54*, 1–22. [[CrossRef](#)]
27. Zhou, T.F.; Yue, S.C.; Yuan, F. *Lithogenesis of Diorites and Copper, Gold Mineralization in Yueshan Orefield, Anhui Province*; Geological Publishing House: Beijing, China, 2005; pp. 1–186.
28. Wang, Q.; Xu, J.; Zhao, Z.; Bao, Z.; Xu, W.; Xiong, X. Cretaceous high-potassium intrusive rocks in the Yueshan-Hongzhen area of east China: Adakites in an extensional tectonic regime within a continent. *Geochem. J.* **2004**, *38*, 417–434. [[CrossRef](#)]
29. Zhao, Z.F.; Zheng, Y.; Wei, C.; Gong, B. Temporal relationship between granite cooling and hydrothermal uranium mineralization at Dalongshan in China: A combined radiometric and oxygen isotopic study. *Ore Geol. Rev.* **2004**, *25*, 221–236. [[CrossRef](#)]
30. Liu, S.A.; Li, S.; He, Y.; Huang, F. Geochemical contrasts between early Cretaceous ore-bearing and ore-barren high-Mg adakites in central-eastern China: Implications for petrogenesis and Cu-Au mineralization. *Geochim. Et Cosmochim. Acta* **2010**, *74*, 7160–7178. [[CrossRef](#)]
31. Yang, Y.Z.; Chen, F.; Siebel, W.; Zhang, H.; Long, Q.; He, J.; Hou, Z.; Zhu, X. Age and composition of Cu-Au related rocks from the lower Yangtze River belt: Constraints on paleo-Pacific slab roll-back beneath eastern China. *Lithos* **2014**, *202*, 331–346. [[CrossRef](#)]
32. Xing, F.M.; Xu, X. High-potassium calc-alkaline intrusive rocks in Tongling area, Anhui province. *Geochimica* **1996**, *25*, 29–38, (In Chinese with English Abstract).
33. Zhang, L.J.; Zhou, T.; Yuan, F.; Fan, Y.; Cooke, D. Petrogenetic-metallogenetic setting and temporal-spatial framework of the Yueshan district, Anhui Province, east-central China. *Int. Geol. Rev.* **2011**, *53*, 542–561. [[CrossRef](#)]
34. Mao, J.W.; Xie, G.; Duan, C.; Pirajno, F.; Ishiyama, D.; Chen, Y. A tectono-genetic model for porphyry-skarn-stratabound Cu-Au-Mo-Fe and magnetite-apatite deposits along the Middle-Lower Yangtze River Valley, Eastern China. *Ore Geol. Rev.* **2011**, *43*, 294–314. [[CrossRef](#)]
35. Xing, F.M.; Xu, X.; Li, Z.C. Discovery of the Early Proterozoic Basement in the Middle-Lower Reaches of Yangtze-River and Its Significance. *Chin. Sci. Bull.* **1994**, *39*, 135–139.
36. Zhou, T.F.; Yuan, F.; Yue, S.; Liu, X.; Zhang, X.; Fan, Y. Geochemistry and evolution of ore-forming fluids of the Yueshan Cu-Au skarn- and vein-type deposits, Anhui Province, South China. *Ore Geol. Rev.* **2007**, *31*, 279–303. [[CrossRef](#)]
37. Anhui, R.G.S. *Regional Geology of Anhui Province*; Geological Publishing House: Beijing, China, 1987; pp. 1–721.
38. Wiedenbeck, M.; Alle, P.; Griffin, W. Three Natural Zircon Standards for U-TH-PB, LU-HF, trace element and ree analyses. *Geostand. Newslett.* **1995**, *19*, 1–23. [[CrossRef](#)]
39. Andersen, T. Correction of common lead in U-Pb analyses that do not report Pb-204. *Chem. Geol.* **2002**, *192*, 59–79. [[CrossRef](#)]
40. Ludwig, K.R. *ISOPLLOT 3.00: A Geochronological Toolkit for Microsoft Excel*; Berkeley Geochronology Center: Berkeley, CA, USA, 2003; pp. 1–39.
41. Wu, F.Y.; Yang, Y.; Xie, L.; Yang, J.; Xu, P. Hf isotopic compositions of the standard zircons and baddeleyites used in U-Pb geochronology. *Chem. Geol.* **2006**, *234*, 105–126. [[CrossRef](#)]
42. Scherer, E.; Munker, C.; Mezger, K. Calibration of the lutetium-hafnium clock. *Science* **2001**, *293*, 683–687. [[CrossRef](#)] [[PubMed](#)]
43. Blichert-Toft, J.; Albarede, F. The Lu-Hf isotope geochemistry of chondrites and the evolution of the mantle-crust system. *Earth Planet. Sci. Lett.* **1997**, *148*, 243–258. [[CrossRef](#)]
44. Griffin, W.L.; Pearson, N.; Belousova, E. The Hf isotope composition of cratonic mantle: LAM-MC-ICPMS analysis of zircon megacrysts in kimberlites. *Geochim. Et Cosmochim. Acta* **2000**, *64*, 133–147. [[CrossRef](#)]
45. Griffin, W.L.; Wang, X.; Jackson, S. Zircon chemistry and magma mixing, SE China: In-situ analysis of Hf isotopes, Tonglu and Pingtan igneous complexes. *Lithos* **2002**, *61*, 237–269. [[CrossRef](#)]
46. Liu, Y.C.; Gu, X.; Li, S.; Hou, Z.; Song, B. Multistage metamorphic events in granulitized eclogites from the North Dabie complex zone, central China: Evidence from zircon U-Pb age, trace element and mineral inclusion. *Lithos* **2011**, *122*, 107–121. [[CrossRef](#)]

47. Yuan, H.L.; Gao, S.; Liu, X.; Li, H.; Gunther, D. Accurate U-Pb age and trace element determinations of zircon by laser ablation-inductively coupled plasma-mass spectrometry. *Geostand. Geoanal. Res.* **2004**, *28*, 353–370. [[CrossRef](#)]
48. Zhang, B.T.; Zhang, F.; Ni, Q.; Chen, P.; Ze, J.; Shen, W. Geology and Geochemical Characteristics of the Anqing-Lujiang Quartz Syenite Rock-belt and its Genesis. *Acta Petrol. Sin.* **1988**, *3*, 1–14, (In Chinese with English Abstract).
49. Qiu, R.L. Petrological characteristics and genesis of High-K diorite in Yueshan, Anhui province. *Geol. Rev.* **1992**, *38*, 97–108, (In Chinese with English Abstract).
50. Zhou, T.F.; Yue, S.; Yuan, F.; Liu, X. A discussion on petrological characteristics and genesis of Yueshan intrusion, Anhui Province. *Geol. J. China Univ.* **2001**, *7*, 70–80, (In Chinese with English Abstract).
51. Yang, G.S.; Wen, H.; Hu, R.; Yu, W.; Fan, H. Petro-geochemical characteristics and genesis of Yueshan intrusion, Anhui province. *Acta Mineral. Sin.* **2007**, *27*, 406–413, (In Chinese with English Abstract).
52. Xu, F.M.; Du, Y.; Wang, G.; Gao, Y.; Dong, Q.; Fang, F. Zircon SHRIMP U-Pb ages, geochemical characteristics and geological implication of Yueshan complex, Anhui province, China. *J. Mineral. Petrol.* **2012**, *32*, 61–66, (In Chinese with English Abstract).
53. Wilson, M. *Igneous Petrogenesis: A Global Tectonic Approach*; Unwin and Hyman: London, UK, 1989; pp. 1–466.
54. Peccerillo, A.; Taylor, S.R. Geochemistry of Eocene calc-alkaline volcanic rocks from the Kastamonu area, Northern Turkey. *Contrib. Mineral. Petrol.* **1976**, *58*, 63–81. [[CrossRef](#)]
55. McDonough, W.F.; Sun, S.S. The Composition of the Earth. *Chem. Geol.* **1995**, *120*, 223–253. [[CrossRef](#)]
56. Watson, E.B.; Harrison, T.M. Zircon saturation revisited: Temperature and composition effects in a variety of crustal magma types. *Earth Planet. Sci. Lett.* **1983**, *64*, 295–304. [[CrossRef](#)]
57. Hofmann, A.W. Chemical Differentiation of the Earth—The Relationship Between Mantle, Continental-Crust, and Oceanic-Crust. *Earth Planet. Sci. Lett.* **1988**, *90*, 297–314. [[CrossRef](#)]
58. Gao, S.; Luo, T.; Zhang, B.; Zhang, H.; Han, Y.; Zhao, Z.; Hu, Y. Chemical composition of the continental crust as revealed by studies in East China. *Geochim. Et Cosmochim. Acta* **1998**, *62*, 1959–1975. [[CrossRef](#)]
59. Hoskin, P.W.O.; Black, L.P. Metamorphic zircon formation by solid-state recrystallization of protolith igneous zircon. *J. Metamorph. Geol.* **2000**, *18*, 423–439. [[CrossRef](#)]
60. Watson, E.B.; Wark, D.A.; Thomas, J.B. Crystallization thermometers for zircon and rutile. *Contrib. Mineral. Petrol.* **2006**, *151*, 413–433. [[CrossRef](#)]
61. Chen, J.F.; Li, X.; Zhou, T.; Foland, K. <sup>40</sup>Ar/<sup>39</sup>Ar dating for the Yueshan diorite, Anhui province and the estimated formation time of the associated ore deposit. *Geoscience* **1991**, *5*, 91–99, (In Chinese with English Abstract).
62. Li, B.; Chen, J.; Zheng, Y.; Zhao, Z.; Qian, H. Relationship among oxygen isotope, Rb-Sr isochron and mineral alteration in quartz diorite at Yueshan in Anhui. *Acta Petrol. Sin.* **2004**, *20*, 1185–1192.
63. Wu, F.Y.; Ji, W.; Sun, D.; Yang, Y.; Li, X. Zircon U-Pb geochronology and Hf isotopic compositions of the Mesozoic granites in southern Anhui Province, China. *Lithos* **2012**, *150*, 6–25. [[CrossRef](#)]
64. Wang, Q.; McDermott, F.; Xu, J. Cenozoic K-rich adakitic volcanic rocks in the Hohxil area, northern Tibet: Lower-crustal melting in an intracontinental setting. *Geology* **2005**, *33*, 465–468. [[CrossRef](#)]
65. Richards, J.R.; Kerrich, R. Special paper: Adakite-like rocks: Their diverse origins and questionable role in metallogenesis. *Econ. Geol.* **2007**, *102*, 537–576. [[CrossRef](#)]
66. Kamei, A.; Miyake, Y.; Owada, M.; Kimura, J. A pseudo adakite derived from partial melting of tonalitic to granodioritic crust, Kyushu, southwest Japan arc. *Lithos* **2009**, *112*, 615–625. [[CrossRef](#)]
67. Xu, J.F.; Shinjo, R.; Defant, M.; Wang, Q.; Rapp, R. Origin of Mesozoic adakitic intrusive rocks in the Ningzhen area of east China: Partial melting of delaminated lower continental crust? *Geology* **2002**, *30*, 1111–1114. [[CrossRef](#)]
68. Rapp, R.P.; Shimizu, N.; Norman, M.; Applegate, G. Reaction between slab-derived melts and peridotite in the mantle wedge: Experimental constraints at 3.8 GPa. *Chem. Geol.* **1999**, *160*, 335–356. [[CrossRef](#)]
69. Chen, J.F.; Zhou, T.; Li, X.; Foland, K.; Huang, C.; Lu, W. Sr and Nd isotopic constraints on source regions of the intermediate and acid intrusions from southern Anhui province. *Geochemistry* **1993**, *3*, 261–268.
70. Defant, M.J.; Kepezhinskis, P. Evidence suggests slab melting in arc magmas. *Trans. Am. Geophys. Union* **2001**, *82*, 65–69. [[CrossRef](#)]

71. Wang, Q.; Wyman, D.; Xu, J.; Jian, P.; Zhao, Z.; Li, C.; Xu, W.; Ma, J.; He, B. Early Cretaceous adakitic granites in the Northern Dabie Complex, central China: Implications for partial melting and delamination of thickened lower crust. *Geochim. Et Cosmochim. Acta* **2007**, *71*, 2609–2636. [[CrossRef](#)]
72. He, Y.S.; Li, S.; Hoefs, J.; Huang, F.; Liu, S.; Hou, Z. Post-collisional granitoids from the Dabie orogen: New evidence for partial melting of a thickened continental crust. *Geochim. Et Cosmochim. Acta* **2011**, *75*, 3815–3838. [[CrossRef](#)]
73. Guo, F.; Fan, W.M.; Li, C.W. Geochemistry of late Mesozoic adakites from the Sulu belt, eastern China: Magma genesis and implications for crustal recycling beneath continental collisional orogens. *Geol. Mag.* **2006**, *143*, 1–13. [[CrossRef](#)]
74. Yan, J.; Chen, J.F.; Xu, X.S. Geochemistry of Cretaceous mafic rocks from the Lower Yangtze region, eastern China: Characteristics and evolution of the lithospheric mantle. *J. Asian Earth Sci.* **2008**, *33*, 177–193. [[CrossRef](#)]
75. Hofmann, A.W. Sampling mantle heterogeneity through oceanic basalts: Isotopes and trace elements. In *The Mantle and Core. Treatise on Geochemistry*; Carlson, R.W., Ed.; Elsevier-Pergamon: Oxford, UK, 2003; pp. 61–101.
76. Jahn, B.M.; Wu, F.; Lo, C.; Tsan, C. Crust-mantle interaction induced by deep subduction of the continental crust: Geochemical and Sr-Nd isotopic evidence from post-collisional mafic-ultramafic intrusions of the northern Dabie complex, central China. *Chem. Geol.* **1999**, *157*, 119–146. [[CrossRef](#)]
77. Ballard, J.R.; Palin, J.M.; Campbell, I.H. Relative oxidation states of magmas inferred from Ce(IV)/Ce(III) in zircon: Application to porphyry copper deposits of Northern Chile. *Contrib. Mineral. Petrol.* **2002**, *144*, 347–364. [[CrossRef](#)]
78. Li, S.; Yang, X.; Huang, Y.; Sun, W. Petrogenesis and mineralization of the Fenghuangshan skarn Cu-Au deposit, Tongling ore cluster field, Lower Yangtze metallogenic belt. *Ore Geol. Rev.* **2014**, *58*, 148–162. [[CrossRef](#)]
79. Tang, M.; Wang, X.; Xu, X.; Zhu, C.; Cheng, T.; Yu, Y. Neoproterozoic subducted materials in the generation of Mesozoic Luzong volcanic rocks: Evidence from apatite geochemistry and Hf-Nd isotopic decoupling. *Gondwana Res.* **2012**, *21*, 266–280. [[CrossRef](#)]
80. Sun, W.H.; Zhou, M.; Gao, J.; Yang, Y.; Zhao, X.; Zhao, J. Detrital zircon U-Pb geochronological and Lu-Hf isotopic constraints on the Precambrian magmatic and crustal evolution of the western Yangtze Block, SW China. *Precambrian Res.* **2009**, *172*, 99–126. [[CrossRef](#)]
81. Xing, F.M.; Xu, X. Two A-type granite belts from Anhui. *Acta Mineral. Sin.* **1994**, *10*, 357–369, (In Chinese with English Abstract).
82. Frost, B.R.; Barnes, C.; Collins, W.; Arculus, R.; Ellise, D.; Frost, C. A geochemical classification for granitic rocks. *J. Petrol.* **2001**, *42*, 2033–2048. [[CrossRef](#)]
83. Frost, C.D.; Frost, B.R. On Ferroan (A-type) Granitoids: Their Compositional Variability and Modes of Origin. *J. Petrol.* **2011**, *52*, 39–53. [[CrossRef](#)]
84. Turner, S.P.; Foden, J.D.; Morrison, R.S. Derivation of Some a-Type Magmas by Fractionation of Basaltic Magma—An Example from the Padthaway Ridge, South Australia. *Lithos* **1992**, *28*, 151–179. [[CrossRef](#)]
85. Wong, J.; Sun, M.; Xing, G.; Li, X.; Zhao, G.; Wong, K.; Yuan, C.; Xia, X.; Li, L.; Wu, F. Geochemical and zircon U-Pb and Hf isotopic study of the Baijuehuan metaluminous A-type granite: Extension at 125–100 Ma and its tectonic significance for South China. *Lithos* **2009**, *112*, 289–305. [[CrossRef](#)]
86. Jiang, Y.; Zhao, P.; Zhou, Q.; Liao, S.; Jin, G. Petrogenesis and tectonic implications of Early Cretaceous S- and A-type granites in the northwest of the Gan-Hang rift, SE China. *Lithos* **2011**, *121*, 55–73. [[CrossRef](#)]
87. Richards, J.P. Postsubduction porphyry Cu-Au and epithermal Au deposits: Products of remelting of subduction-modified lithosphere. *Geology* **2009**, *37*, 247–250.
88. Richards, J.P. Magmatic to hydrothermal metal fluxes in convergent and collided margins. *Ore Geol. Rev.* **2011**, *40*, 1–26.
89. Mao, J.W.; Wang, Y.; Lehmann, B.; Yu, J.; Du, A.; Mei, Y. Molybdenite Re-Os and albite Ar-40/Ar-39 dating of Cu-Au-Mo and magnetite porphyry systems in the Yangtze River valley and metallogenic implications. *Ore Geol. Rev.* **2006**, *29*, 307–324. [[CrossRef](#)]
90. Brandon, A.D.; Draper, D.S. Constraints on the origin of the oxidation state of mantle overlying subduction zones: An example from Simcoe, Washington, USA. *Geochim. Et Cosmochim. Acta* **1996**, *60*, 1739–1749. [[CrossRef](#)]

91. Sun, W.D.; Liang, H.; Ling, M.; Zhan, M.; Ding, X.; Zhang, H.; Yang, X.; Li, Y.; Ireland, T.; Wei, Q.; et al. The link between reduced porphyry copper deposits and oxidized magmas. *Geochim. Et Cosmochim. Acta* **2013**, *103*, 263–275. [[CrossRef](#)]
92. Sun, W.D.; Zhang, H.; Ling, M.; Ding, X.; Chung, S.; Zhou, J.; Yang, X.; Fan, W. The genetic association of adakites and Cu-Au ore deposits. *Int. Geol. Rev.* **2011**, *53*, 691–703. [[CrossRef](#)]
93. Moghadam, H.S.; Rossetti, F.; Lucci, F.; Chiaradia, M.; Gerdes, A.; Martinez, M.; Ghorbani, G.; Nasrabad, M. The calc-alkaline and adakitic volcanism of the Sabzevar structural zone (NE Iran): Implications for the Eocene magmatic flare-up in Central Iran. *Lithos* **2016**, *248*, 517–535. [[CrossRef](#)]
94. Rossetti, F.; Nasrabad, M.; Theye, T.; Gerdes, A.; Monie, P.; Lucci, F.; Vignaroli, G. Adakite differentiation and emplacement in a subduction channel: The late Paleocene Sabzevar magmatism (NE Iran). *Geol. Soc. Am. Bull.* **2014**, *126*, 317–343. [[CrossRef](#)]
95. Min, M.Z.; Luo, X.; Du, G.; He, B.; Campbell, A. Mineralogical and geochemical constraints on the genesis of the granite-hosted Huangao uranium deposit, SE China. *Ore Geol. Rev.* **1999**, *14*, 105–127. [[CrossRef](#)]
96. Deng, G.R. A brief analysis of geological features of the Dalongshan uranium ore deposit formation in Anqing. *Geol. Anhui* **2017**, *27*, 95–98, (In Chinese with English Abstract).



© 2018 by the authors. Licensee MDPI, Basel, Switzerland. This article is an open access article distributed under the terms and conditions of the Creative Commons Attribution (CC BY) license (<http://creativecommons.org/licenses/by/4.0/>).